remote sensing

MDPI

Article

Assessment of Post-Fire Impacts on Vegetation Regeneration and Hydrological Processes in a Mediterranean Peri-Urban Catchment

Evgenia Koltsida [1], Nikos Mamassis [2], Evangelos Baltas [2], Vassilis Andronis [3] and Andreas Kallioras [1,*]

[1] Laboratory of Engineering Geology and Hydrogeology, School of Mining and Metallurgical Engineering, National Technical University of Athens, Heroon Polytechniou 9, Zografou, 157 80 Athens, Greece; ekoltsida@metal.ntua.gr
[2] Laboratory of Hydrology and Water Resources Development, School of Civil Engineering, National Technical University of Athens, Heroon Polytechniou 9, Zografou, 157 80 Athens, Greece; nikos@itia.ntua.gr (N.M.); baltas@mail.ntua.gr (E.B.)
[3] Laboratory of Remote Sensing, School of Rural and Surveying Engineering, National Technical University of Athens, Heroon Polytechniou 9, Zografou, 157 80 Athens, Greece; andronis@central.ntua.gr
* Correspondence: kallioras@metal.ntua.gr; Tel.: +30-210-772-2098

Abstract: This study aimed to evaluate the impact of a wildfire on vegetation recovery and hydrological processes in a Mediterranean peri-urban system, using remote sensing and hydrological modeling. NDVI and $MSAVI_2$ time series extracted from burned areas, control plots, and VAR-modeled plots were used to analyze vegetation regeneration. The SWAT model, calibrated for pre-fire conditions due to data limitations, was used to evaluate subbasin-scale hydrological impacts. Results showed limited recovery in the first post-fire year, with vegetation indices remaining lower in burned areas compared to control plots. High- and moderate-burn-severity areas presented the most significant NDVI and $MSAVI_2$ increases. The SWAT model showed increased water yield, percolation, and surface runoff with reduced evapotranspiration in post-fire conditions. Peak discharges were notably higher during wet periods. Modified land use and soil properties affected the catchment's hydrological balance, emphasizing the complexities of post-fire catchment dynamics.

Keywords: hydrological processes; hydrological modeling; SWAT; wildfire; experimental catchment; remote sensing

Citation: Koltsida, E.; Mamassis, N.; Baltas, E.; Andronis, V.; Kallioras, A. Assessment of Post-Fire Impacts on Vegetation Regeneration and Hydrological Processes in a Mediterranean Peri-Urban Catchment. *Remote Sens.* **2024**, *16*, 4745. https://doi.org/10.3390/rs16244745

Academic Editor: Hatim Sharif

Received: 15 November 2024
Revised: 13 December 2024
Accepted: 16 December 2024
Published: 19 December 2024

1. Introduction

Wildfires are a significant environmental issue, particularly in Mediterranean climate catchments, where they are widespread and often lead to severe land use and soil changes, affecting hydrological processes [1,2]. These alterations can reduce vegetation and ground cover and alter soil properties, and increase soil susceptibility to runoff, leading to important economic and environmental consequences [3–7]. Furthermore, soil water repellency due to the loss of the topsoil organic matter leads to reduced infiltration and storage capacity, alongside increased overland flow [8–10]. Wildfire recurrence can also contribute to soil degradation and desertification [11,12].

Vegetation regeneration following wildfires is crucial for mitigating these impacts, and remote sensing techniques can provide valuable insights into post-fire vegetation dynamics [13]. Information on burn severity and vegetation recovery offers insight into how several vegetation categories respond to fire and can identify areas requiring intensive restoration to minimize the consequences of soil erosion and increased runoff [14,15]. Spectral vegetation indices enable the assessment of vegetation dynamics across multiple scales and have been extensively used to monitor changes in vegetation cover [16]. The vegetation indices are estimated from remote sensing reflectance measurements in the visible and infrared regions of the electromagnetic spectrum. The Normalized Difference

Vegetation Index (NDVI) [17] has been extensively used to detect vegetation regeneration and has been applied to several diverse environments [2,14,18]. Huete et al. [19] proposed the Soil-Adjusted Vegetation Index (SAVI) to overcome problems of the $NDVI$ with soil background variations. Qi et al. [20] suggested the $MSAVI_2$, which reduces soil background noise and enhances vegetation signal in satellite images more effectively than the SAVI [21–23]. The Normalized Burn Ratio (NBR) [24] has also been used to assess burn severity, monitor vegetation recovery, and describe physical changes caused by fires [15,25–29]. Additionally, forecasting models [30–33] and vegetation indices from unburned control plots [11,34–37] provide useful tools for estimating fire impacts and quantifying vegetation recovery, especially in the absence of field data. Combining multiple remote sensing techniques, forecasting models, and control plots is a more efficient alternative for detecting the spatial and temporal variations in fire effects than relying exclusively on traditional field inventories [26,38,39].

The hydrological response to fire impact is determined by various factors, including burn severity, meteorological conditions, land use, soil properties, topography, and land management practices [6,12]. Hydrological modeling is a valuable tool for quantifying the impact of fires in catchment hydrological processes. It enables the evaluation of the impacts of post-fire conditions on the hydrological cycle and supports management decisions to mitigate surface runoff and soil erosion [40,41]. Post-fire conditions have usually been simulated using empirical models (i.e., the universal soil loss equation, USLE) [42], semi-empirical models (i.e., the revised Morgan–Morgan–Finney model) [43], the Pan-European Soil Erosion Risk Assessment [44], and the Soil and Water Assessment Tool (SWAT) [45]. There is limited research on the relationship between fires and hydrological processes in burnt Mediterranean areas due to the absence of catchment-scale data [8]. In particular, for the Mediterranean area, hydrological models have mostly been applied at the field scale [12,40,46–48] and rarely at the catchment scale [3,4,49,50]. The catchment scale provides valuable information about the different mechanisms controlling surface runoff, which is essential for planning post-fire soil rehabilitation [4,5,40]. However, model calibration and validation under post-fire conditions at this scale is challenging due to the absence of observed hydro-meteorological data [10,13,49].

During July and August 2021, one of the most intense wildfires in Greece occurred, which was unprecedented in extent, intensity, and impact, with a total burned area of 3600 km^2 [51–54]. This study employed remote sensing techniques and hydrological modeling to estimate the post-fire vegetation regeneration and hydrological impacts of the 2021 wildfire in the Kifisos experimental subbasin, Attica, Greece. The study area constituted a peri-urban system, i.e., a hybrid landscape in which different land uses such as forests, crops, and urban zones interact. The interaction between different land uses makes this area a constantly changing environment exposed to more significant risks from forest fires and floods and characterized by diverse management practices and hydrological processes. Satellite data from NASA's Landsat 8 (Operational Land Imager, OLI, Ball Aerospace & Technologies Corp., Boulder, CO, USA) were used before and after the fire in July 2021 and August 2021, respectively, and one year later in August 2022 to construct a burn severity map and investigate post-fire vegetation recovery. Landsat-5 imagery (covering the period 1990–2011) and Landsat-8 imagery (covering the period 2013–2022) were also used to assess vegetation regrowth in the study area. In addition, the SWAT model was used to investigate the impact of fire on the catchment's hydrological components. Observed discharge data were available only for the pre-fire conditions. The SWAT model was calibrated and validated for the pre-fire conditions, and post-fire land use and soil changes were applied to incorporate burn severity. Although there have been several prior studies on the hydrological impacts of fires, the innovative aspect of this study lies in its collaborative use of remote sensing techniques, a forecasting model, and a hydrological model (daily and hourly time step) to assess alterations in hydrological parameters before and after the fire event and to evaluate the sub-daily option of the SWAT model for discharge simulation. The objectives of this study were the (i) quantification of

the vegetation recovery dynamics within the burned area using remote sensing techniques, (ii) investigation of the use of control plots and forecasting models, and (iii) assessment of the accuracy of a modeling tool to simulate post-fire conditions and impacts at the catchment scale and evaluate its usefulness as a post-fire management tool.

2. Materials and Methods

2.1. Study Area and Data Description

The study area (Figure 1) was the experimental northwest subbasin of the Kifisos river basin. It occupies an area of 140 km^2 [55] and has an elevation range of 94 to 1399 m. The climate is Mediterranean, with mild, wet winters and hot, dry summers [56]. The mean annual precipitation is 577.2 mm, and the mean annual temperature is 16.4 °C [57]. The area is geologically covered mainly by the Cambisols, Regosols, Leptosols, and Luvisols formations [58]. It is an urban and peri-urban region with residential areas (34.1%), shrubland (15.9%), and agriculture (12.4%) [59].

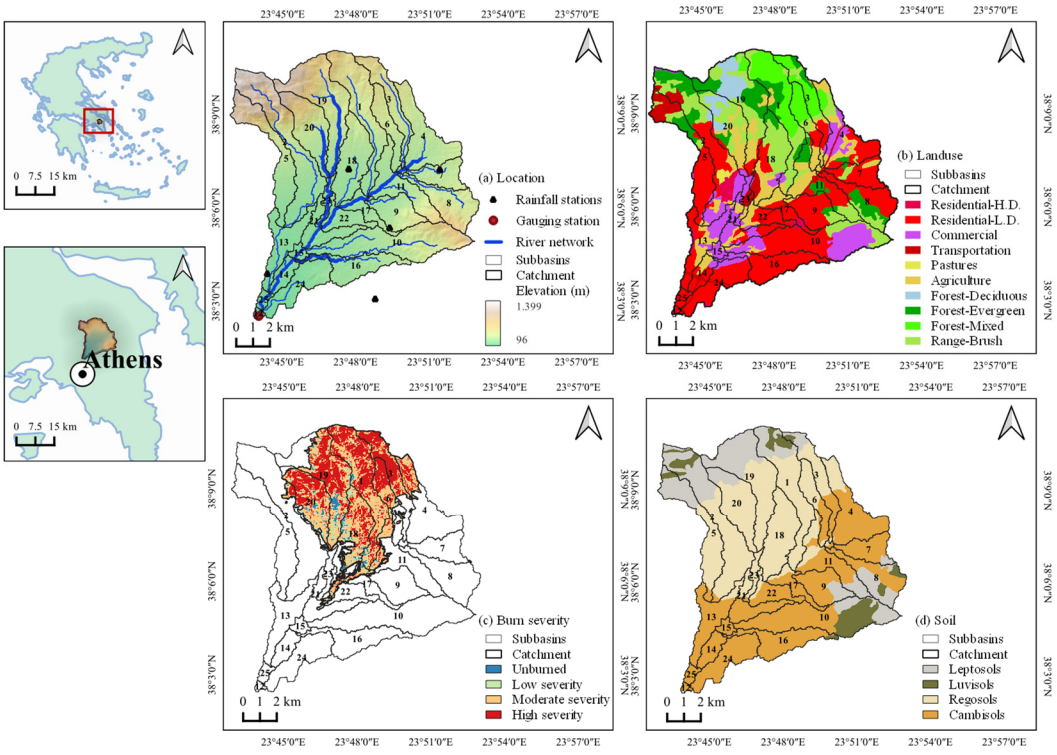

Figure 1. Elevation of the study area (**a**), spatial distribution of land use (**b**), burn severity (**c**), and soil types (**d**). Zoomed-out display of Greece and Athens location in red box (**upper left**) and Athens metropolitan area (**lower left**). The study area includes 25 subbasins, of which the subbasin numbers 1, 2, 3, 4, 6, 11, 17, 18, 19, and 20 indicate the subbasins inside the burn scar.

On 3 August 2021, a forest fire took place in the study area, which lasted for the next few days and impacted 12 subbasins (Figure 1c). The fire primarily impacted the northern part of the study area, which included forest vegetation and a significant portion of the nearby urban areas [54,60]. This wildfire event was used to assess vegetation recovery and its impact on the water balance over one year. Landsat-5 (1990–2011) and Landsat-8 (2013–2022) imagery was used to investigate vegetation regrowth before and after the fire. The Landsat images were processed to calculate the mean monthly $NDVI$ and $MSAVI_2$ values for each subbasin and land use category at a 30 m spatial resolution. In addition, images before and after the fire in July 2021 and August 2021, respectively, and one year later in August 2022 were used to map burn severity. The unburned subbasins (ID: 5, 8, 10) and minimally affected subbasins (ID: 2, 3, 4, 11, 19) were used as control subbasins. The

control subbasins shared the same geomorphological and vegetation characteristics with the burned subbasins to ensure their comparability [11,34–37].

Furthermore, a hydrological model was developed to analyze the influence of post-fire conditions on the hydrological cycle. The input data for the model included a digital elevation model (DEM) with 30 m resolution from the website of the U.S. Geological Survey [61], a land use map with 100 m resolution from the Corine Land Cover map [59], a soil map from the Food and Agriculture Organization (FAO)'s Digital Soil Map of the World [58], meteorological data covering the period from 2017 to 2022 (i.e., rainfall, temperature, wind speed, relative humidity, and solar radiation) [57], and observed discharge data available from 1 January 2018 to 31 March 2020 [62].

2.2. Burn Severity Mapping and Post-Fire Vegetation Recovery

The analysis of the burn severity and vegetation recovery of the study area was performed using the Google Earth Engine (GEE) platform. GEE is a free cloud-based platform for planetary-scale geospatial analysis [63]. Registered users can access GEE through two web-based platforms: the GEE Explorer and Code Editor. The GEE Explorer allows users to view satellite imagery, while the GEE Code Editor enables analysis and customization through coding.

The Landsat datasets (i.e., Landsat-5 and Landsat-8) were obtained from the U.S. Geological Survey (USGS), covering two time periods, (a) 1990–2011 (from January 1990 to September 2011) and (b) 2013–2022 (from May 2013 to September 2022). These products are available in GEE as LANDSAT/LT05/C02/T1_TOA and LANDSAT/LC08/C02/T1_TOA. All satellite images were projected on the reference coordinate system of the study area (WGS 84/UTM zone 36N). A cloud-masking process [64] was conducted using the pixel quality assessment band to identify cloud-affected pixels. Composites for pre- and post-fire periods using median values over a specific time range were finally created, resulting in 125 images from Landsat-5 and 69 images from Landsat-8.

The identification of burned areas and the estimation of burn severity [15] were performed using the Normalized Burn Ratio (NBR) [24] for both pre-fire and post-fire conditions. The NBR is a ratio between the near-infrared (NIR) (i.e., burned areas showing low reflectance) and the short-wave infrared ($SWIR$) (i.e., burned areas showing high reflectance) spectral bands [65]. The index presents high values in areas with healthy vegetation and low values in burned regions or those with sparse vegetation [66]. The index is estimated by (Equation (1)):

$$NBR = \frac{NIR - SWIR}{NIR + SWIR} \quad (1)$$

where NIR is the near-infrared band (Landsat 4–7 band 4; Landsat 8–9 band 5) and $SWIR$ is the short-wave infrared band (Landsat 4–7 band 7; Landsat 8–9 band 7), respectively.

The NBR index calculated for post-fire conditions was subtracted from the NBR index calculated for pre-fire conditions to provide a scaled index of burn severity, known as the Differenced Normalized Burn Ratio, delta NBR, or $dNBR$ [24]. Generally, unburned areas show $dNBR$ values near zero, and burned areas show high positive $dNBR$ values. The $dNBR$ is calculated by (Equation (2)):

$$dNBR = NBR_{prefire} - NBR_{postfire} \quad (2)$$

where $NBR_{prefire}$ is the NBR index for pre-fire conditions and $NBR_{postfire}$ is the NBR index for post-fire conditions.

Furthermore, the assessment of the vegetation recovery was achieved using the Normalized Difference Vegetation Index (NDVI) [17] and the Modified Soil-Adjusted Vegetation Index ($MSAVI_2$) [20]. $NDVI$ values range between -1 and 1, where zero to negative values indicate areas with a lack of vegetation [67]. A study by [19] proposed the Soil-Adjusted Vegetation Index (SAVI) to overcome problems of the $NDVI$ with soil background varia-

tions. The $MSAVI_2$ offers a stronger reduction in the soil noise influences than the SAVI [20]. Both the $NDVI$ (Equation (3)) and $MSAVI_2$ (Equation (4)) are calculated using the red (RED) and near-infrared (NIR) spectral bands, as follows:

$$NDVI = \frac{NIR - RED}{NIR + RED} \tag{3}$$

$$MSAVI_2 = \frac{2 \times NIR + 1 - \sqrt{(2 \times NIR + 1)^2 - 8 \times (NIR - RED)}}{2} \tag{4}$$

where NIR is the near-infrared band (Landsat 4–7 band 4; Landsat 8–9 band 5) and RED is the red band (Landsat 4–7 band 3; Landsat 8–9 band 4), respectively.

For each $NDVI$ and $MSAVI_2$ image, the mean value of the pixels was calculated for each subbasin using a zonal statistics function. Then, the post-fire vegetation indices were compared to the pre-fire indices to analyze the rate of the regeneration process. Finally, descriptive statistics of the $NDVI$ and $MSAVI_2$ were calculated for each satellite image for each land use and burn severity category within the study area to analyze the relationship between vegetation regeneration and burn severity.

2.3. Pre- and Post-Fire Vegetation Indices

Further analysis was performed to compare the differences between the vegetation indices before and after the fire event. The Vector Autoregression (VAR) model [68] was applied to predict $NDVI$ and $MSAVI_2$ time series from 1 August 2021 to 31 January 2023 without the influence of fire. The choice of variables included in the VAR model, specifically the $NDVI$ and $MSAVI_2$, was driven by their relevance to monitoring vegetation dynamics. These indices are sensitive to changes in vegetation cover and health, making them ideal for assessing post-fire recovery and the impact of fire on vegetation.

The Vector Autoregressive (VAR) model is a multivariate linear time series model used to capture the interdependencies between multiple time series influencing variables [68]. It is particularly well suited for analyzing multiple interdependent time series data, such as the $NDVI$ and $MSAVI_2$, simultaneously. This is crucial for understanding the complex interdependencies between these indices and other environmental variables affecting post-fire vegetation recovery. Also, the VAR model provides a systematic approach to capturing the dynamic interactions between multiple time series by incorporating the lagged values of all the variables into each equation. This allows for a comprehensive assessment of how past values of each variable influence future outcomes, which is essential for accurately modeling and forecasting the ecological impacts of wildfires [69].

The VAR model is the generalized form of the univariate autoregressive model for forecasting a time series vector [70]. Each variable in the VAR model is defined by an equation that includes the variable's lagged values and the lagged values of all the other variables in the model [71]. The general VAR (P) model is mathematically expressed using the following equation (Equation (5)):

$$y_t = c + A_1 y_{t-1} + A_2 y_{t-2} + \cdots + A_p y_{t-p} + e_t \tag{5}$$

where y_t, $t = 1, \ldots, T$, is a $k \times 1$ vector of the time series, c is a k-vector of constants, A_i is a $k \times k$ parametric matrix, and e_t represents a k-vector of error terms.

The R programming language was used to develop a forecasting model and conduct time series analysis on the monthly Landsat dataset covering the period from 1990 to 2022. First, the Kalman smoothing filter [72] was used to address missing values in the dataset. The VAR model requires that all the time series data be stationary. To assess stationarity, the Augmented Dickey–Fuller (ADF) test [73] was used. Then, the optimal lag length for the model was selected by looking at the minimum values of the following criteria: the Final Prediction Error Correction (FPE), the Akaike Information Criterion (AIC), the Schwarz Information Criterion (SIC), and the Hannan–Quinn Information Criterion (HQ).

Finally, this was followed by residual analysis testing for normality, heteroscedasticity, and autocorrelation.

The time series derived from the forecasting model were further compared with unburned control plot values. Unburned subbasins (ID: 5, 8, 10) and minimally affected subbasins (ID: 2, 3, 4, 11, 19) close to the study area with similar environmental and land use conditions were selected as control subbasins (Figure 1). Mean $NDVI$ and $MSAVI_2$ values for each land use were extracted from the control subbasins and compared to the pre-fire and post-fire patterns. The $NDVI$ and $MSAVI_2$ values derived from unburned control subbasins, along with values from the VAR model, provide an essential tool for assessing the impact of fire and the subsequent regrowth of vegetation. The application of a VAR model in this study provides a robust analytical framework that not only predicts future states of vegetation indices, but also aids understanding of the temporal interactions and dependencies between the variables studied. This approach has value in ecological studies where multiple factors interact in complex ways over time.

2.4. Hydrological Model

2.4.1. Model Conceptual Framework

The SWAT (Soil and Water Assessment Tool) model [74] was used to assess the impact of fire on the hydrological cycle of the study area. The SWAT model is an open-source, physically based, continuous-time river basin model designed to analyze the effects of management practices on discharge, sediment transport, and agricultural activities in large and complex watersheds [75]. The main elements of the SWAT model include hydrology, weather, soil, land use, sediments, nutrients, bacteria, and pathogens [76,77].

The water balance equation is estimated using the following equation (Equation (6)):

$$SW_t = SW_o + \sum_{i=1}^{t} \left(R_{day} - Q_{surf} - E_a - W_{seep} - Q_{gw} \right) \quad (6)$$

where SW_t is the soil water content (mm), SW_o is the soil water content on day i in the previous period (mm), t is the time step (days), R_{day} indicates the amount of precipitation on day i (mm), Q_{surf} represents the surface streamflow on day i (mm), E_a indicates the AET on day i (mm), W_{seep} is the percolation and bypass flow on day i (mm), and Q_{gw} represents the return flow on day i (mm).

First, the SWAT model was set up with two different scenarios covering the pre-fire (1 January 2018 to 31 July 2021) and the post-fire (1 August 2021 to 31 December 2022) conditions. The QSWAT plugin in the QGIS platform was used for model setup and parameterization [78]. The two scenarios (i.e., pre-fire and post-fire) were applied throughout the study period (1 January 2018 to 31 December 2022) to evaluate the influence of changes in land use and soil properties on the catchment's hydrological behavior. In this way, the hydrological balances of the two scenarios could be compared independently of the influence of meteorological conditions (wet and dry years). In both scenarios, the first year was used for model warm-up. Both scenarios followed the same catchment delineation process, using a drainage area of 3.6 km^2, leading to 25 subbasins. The land use and soil maps were overlaid with the burn severity map. Subsequently, the post-fire maps were reclassified to include low-, moderate-, and high-burn-severity classes. The pre-fire scenario database consisted of the original pre-fire land use and soil attributes, while the post-fire scenario database included new land use and soil lookup tables, which were adjusted to reflect the post-fire conditions. The meteorological information was incorporated in the two scenarios. Potential evapotranspiration was estimated using the Penman–Monteith method, and surface runoff was computed using the curve number (CN) method [79] for the daily model and the Green and Ampt Mein Larson infiltration (GAML) method [80] for the hourly model.

Model calibration and validation were implemented using the Sequential Uncertainty Fitting (SUFI-2) algorithm within the SWAT-CUP software, version 5.2.1.1 [81]. The pre-fire scenario was calibrated from January 2018 to December 2018 and validated from January

2019 to March 2020 using available discharge data. Then, the post-fire scenario (1 August 2021 to 31 December 2022) was calibrated using the values from the pre-fire scenario for areas that were unaffected by the fire. For the regions impacted by the fire, specific parameters were adjusted to reflect post-fire changes in land use and soil conditions. The parameters modified in the post-fire model were the saturated soil hydraulic conductivity (SOL_K), the available water capacity of the soil layer (SOL_AWC), the maximum canopy storage (CHTMX), the crop vegetation factor (USLE_C), the soil erodibility factor (USLE_K), the curve number (CN2), the organic carbon content (SOL_CBN), and the moist bulk density (SOL_BD). The two scenarios were evaluated using statistical (i.e., NSE, R^2, PBIAS) and graphical (i.e., time series charts, maps, percent exceedance probability curves) techniques at daily and hourly spatial scales [82].

2.4.2. Post-Fire Scenario

The parameters for infiltration and surface runoff were modified to reflect post-fire conditions, taking into account the effects of burn severity. In particular, the soil erodibility factor (USLE_K) was increased by 0.014, 0.015, and 0.016 Mg ha−1 MJ−1 mm−1 ha hr for low, moderate, and high burn severity [4,40,83]. The crop vegetation factor (USLE_C) was adjusted to 0.01, 0.05, and 0.2 (−) for low, moderate, and high burn severity [4,40,83]. The curve number (CN2) was increased by 5, 10, and 15 (−) for low, moderate, and high burn severity, respectively [4,29,41]. In addition, the saturated hydraulic conductivity (SOL_K), the soil available water capacity (SOL_AWC), the maximum canopy storage (CHTMX), and the organic matter (SOL_CBN) were slightly reduced, and the bulk density (SOL_BD) was slightly increased [6,7].

The new parameter values were imported into the soil and land use SWAT database, and new lookup tables and maps were created to incorporate the effects of burn severity. These modifications resulted in low-, moderate-, and high-burn-severity areas. In these areas, new HRUs were formed to represent the attribute changes.

3. Results

3.1. Post-Fire Assessment of Vegetation Recovery

3.1.1. Burn Severity

A burn severity map was created using the *NBR* and *dNBR* (The Differenced Normalized Burn Ratio (*dNBR*) was used to quantify the extent and severity of burned areas by comparing pre- and post-fire satellite images. Developed by Key and Benson [24], the *dNBR* combines the Normalized Burn Ratio (*NBR*) index from two different dates to assess the changes in vegetation and surface conditions caused by wildfires. The *dNBR* is widely used for burned area mapping, post-fire severity assessment, and monitoring of vegetation recovery, minimizing the influence of atmospheric conditions and variations in solar angle on the index values [84].) indices (Figure 1c). The burned area (42.67 km^2) was discretized into four burn severity classes using the *dNBR* categories proposed by USGS: (i) unburned (*dNBR* values ranging from −0.1 to 0.1), low severity (0.1 to 0.27), moderate severity (0.27 to 0.66), and high severity (0.66 to 1). Most of the burn scar areas included highly and moderately burned areas. The high-burn-severity class comprised 13.1% of the total study area (140 km^2), followed by the moderate-burn-severity class (14.2%), the low-burn-severity class (3.1%), and the unburned class (69.5%). The land use categories with the most significant percentage of highly burned areas were the mixed forest (FRST) (65.4%), the deciduous forest (FRSD) (50.8%), the evergreen forest (FRSE) (19.6%), and the shrubland (RNGB) (25.7%). The agricultural areas (AGRL) included mainly moderately burned areas (23.6%). The artificial areas (i.e., transportation, green areas, residential low density, and commercial) included low-burn-severity areas (5.9%). In general, twelve subbasins were affected (Figure 1). Subbasin ID = 3 had the highest percentage of high burn severity (49.8%), following subbasin ID = 1 (48.6%) and subbasin ID = 20 (37.4%).

3.1.2. Pre- and Post-Fire Vegetation Dynamics

The dynamics of vegetation regrowth following the fire were assessed through a multi/temporal analysis of the $NDVI$ and $MSAVI_2$ indices. The basic statistics of the $NDVI$ and $MSAVI_2$ time series used in the analysis are presented in Table 1. The highest values of $NDVI$ and $MSAVI_2$ were associated with the land use categories forest—deciduous (FRSD), forest—evergreen (FRSE), and forest—mixed (FRST).

Table 1. First-order statistics of the $NDVI$ and $MSAVI_2$ time series for the period 1990–2021. AGRL, agriculture; FRSD, deciduous forest; FRSE, evergreen forest; FRST, mixed forest; RNGB, shrubland; UCOM, transportation/green areas.

	NDVI						***MSAVI*$_2$**					
Statistics	**AGRL**	**FRSD**	**FRSE**	**FRST**	**RNGB**	**UCOM**	**AGRL**	**FRSD**	**FRSE**	**FRST**	**RNGB**	**UCOM**
Min.	0.170	0.340	0.290	0.320	0.240	0.120	0.100	0.180	0.130	0.150	0.090	0.070
1st Quantile	0.280	0.530	0.410	0.470	0.390	0.170	0.150	0.280	0.180	0.220	0.190	0.100
Median	0.340	0.560	0.440	0.510	0.430	0.220	0.190	0.300	0.190	0.240	0.210	0.130
Mean	0.345	0.564	0.457	0.517	0.427	0.224	0.193	0.307	0.204	0.249	0.213	0.128
3rd Quantile	0.400	0.610	0.520	0.570	0.470	0.260	0.230	0.340	0.240	0.280	0.230	0.150
Max.	0.550	0.680	0.600	0.650	0.560	0.380	0.310	0.430	0.300	0.360	0.320	0.220
Stdev	0.081	0.057	0.063	0.061	0.055	0.060	0.044	0.043	0.034	0.038	0.030	0.034

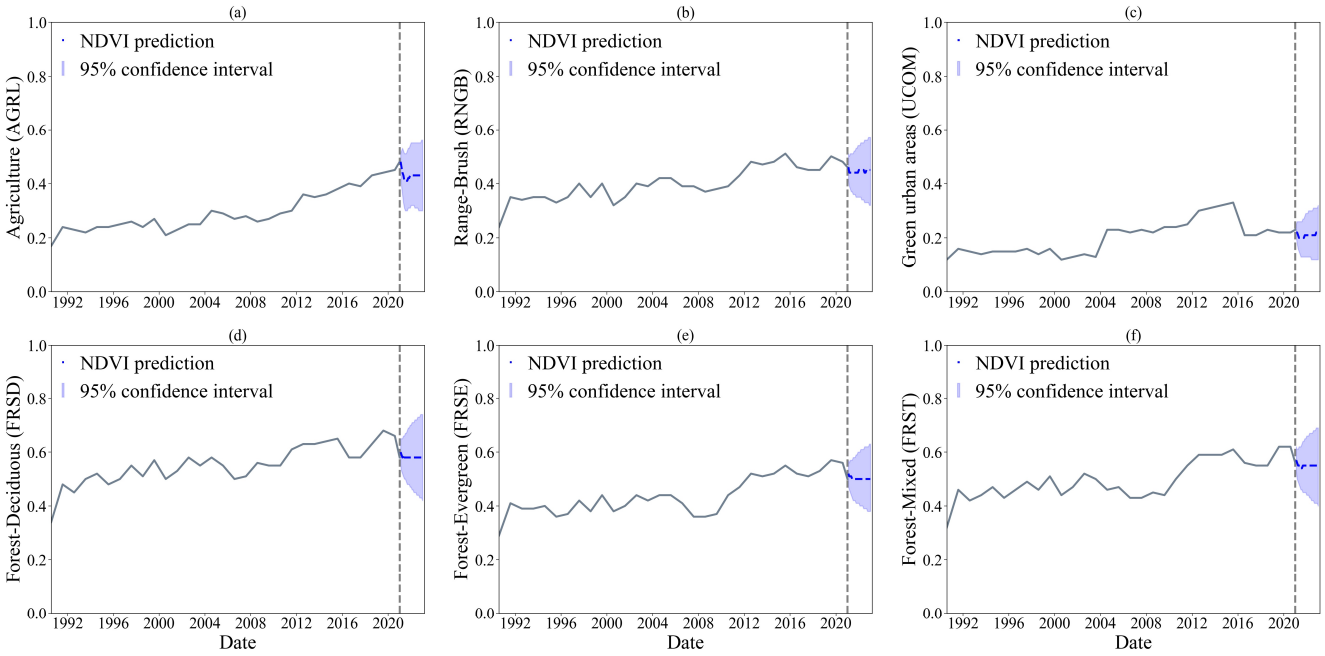

Figure 2. $NDVI$ predictions for the period August 2021 to January 2023 without the influence of fire. (**a**) AGRL, agriculture. (**b**) RNGB, shrubland. (**c**) UCOM, transportation/green areas. (**d**) FRSD, deciduous forest. (**e**) FRSE, evergreen forest. (**f**) FRST, mixed forest.

The Vector Autoregressive (VAR) model was developed using the average values of the $NDVI$ and $MSAVI_2$ from the monthly data. The dataset was divided into two parts: a training time series consisting of data from January 1990 to January 2021 and a testing time series from February 2021 to July 2021. Forecasts for the period from August 2021 to January 2023 were generated based on the training data. The Augmented Dickey–Fuller (ADF) test was performed to determine the stationarity of the time series. The $NDVI$ and $MSAVI_2$ time series for the pre-fire period (1990–2021), shown in Figures 2 and 3, did not exhibit a significant upward or downward trend. The ADF test indicated that the null hypothesis of a unit root could be rejected for all variables at the 5% significance level (p-value < 0.05). Therefore, all the variables could be considered as from stationary time

series and could proceed with the simulation analysis. Additionally, a stability test of the VAR model was conducted to determine whether the parameters change over time. All the characteristic roots were less than one, indicating that the VAR model satisfies the stability condition and shows no structural breaks [85].

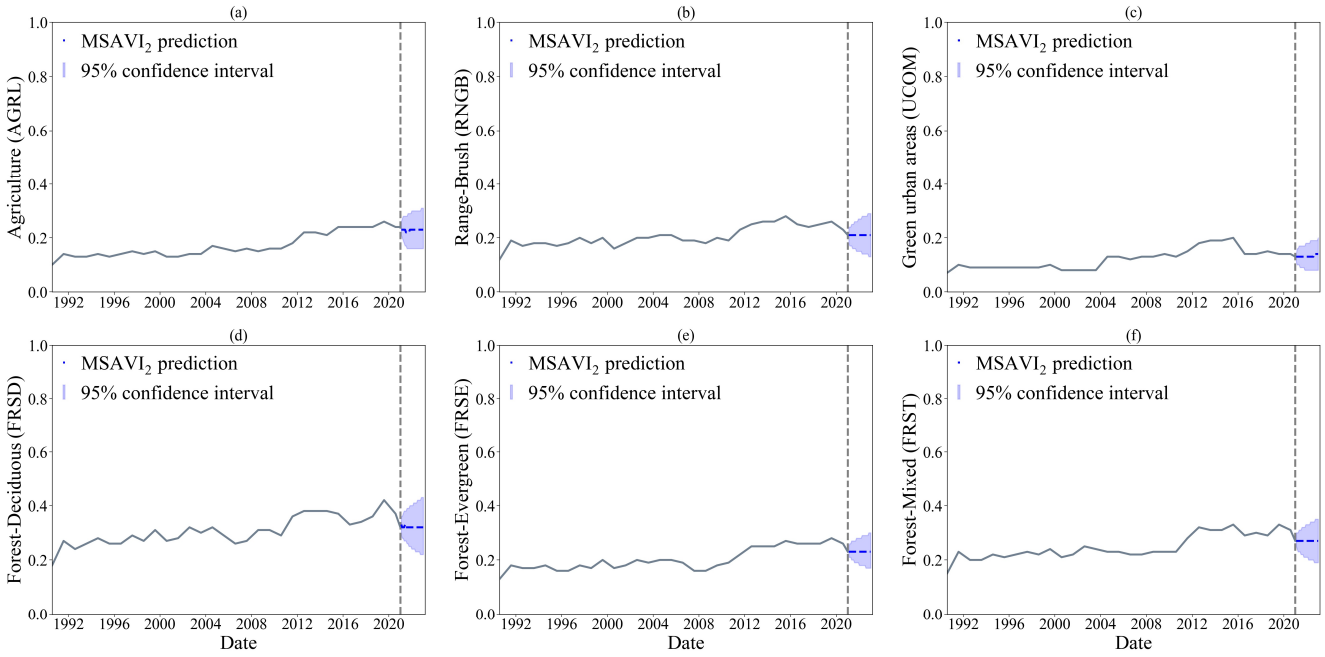

Figure 3. $MSAVI_2$ predictions for the period August 2021 to January 2023 without the influence of fire. (**a**) AGRL, agriculture. (**b**) RNGB, shrubland. (**c**) UCOM, transportation/green areas. (**d**) FRSD, deciduous forest. (**e**) FRSE, evergreen forest. (**f**) FRST, mixed forest.

The time series derived from the Vector Autoregression (VAR) model and the unburned/minimally affected control plots were used to determine fire impact and vegetation regrowth. The mean $NDVI$ and $MSAVI_2$ of the unburned control plots, Vector Autoregression (VAR) model control plots, and burned plots are displayed in Figures 4 and 5. Table 2 presents the mean $NDVI$ and $MSAVI_2$ differences between the burned and control plots for each land use category. In the pre-fire period (August 2016–July 2021), the differences between the values of the burned plots and those of control plots for all land use categories were minimal. The $NDVI_{burned}$ and $MSAVI_{2burned}$ values were mainly below $NDVI_{control}$ and $MSAVI_{2control}$ for five years before the wildfire (Figures 4 and 5, Table 2). Table 1 shows the first-order statistics of the $NDVI$ and $MSAVI_2$ time series for the period 1990–2021. After the fire, the $NDVI_{burned}$ and $MSAVI_{2burned}$ declined substantially for the land use categories FRSD, FRSE, and FRST ($NDVI_{mean}$: FRSD: 0.34, FRSE: 0.37, FRST: 0.26; $MSAVI_{2mean}$: FRSD: 0.18, FRSE: 0.18, FRST: 0.11). Within one year post-fire, the categories AGRL, RNGB, and UCOM showed rapid recovery ($NDVI_{mean}$: AGRL: 0.35, RNGB: 0.46, UCOM: 0.22; $MSAVI_{2mean}$: AGRL: 0.20, RNGB: 0.21, UCOM: 0.14). The $NDVI_{burned}$ and $MSAVI_{2burned}$ values of the categories FRSD, FRSE, and FRST still lagged behind the $NDVI_{control}$ and $MSAVI_{2control}$ values.

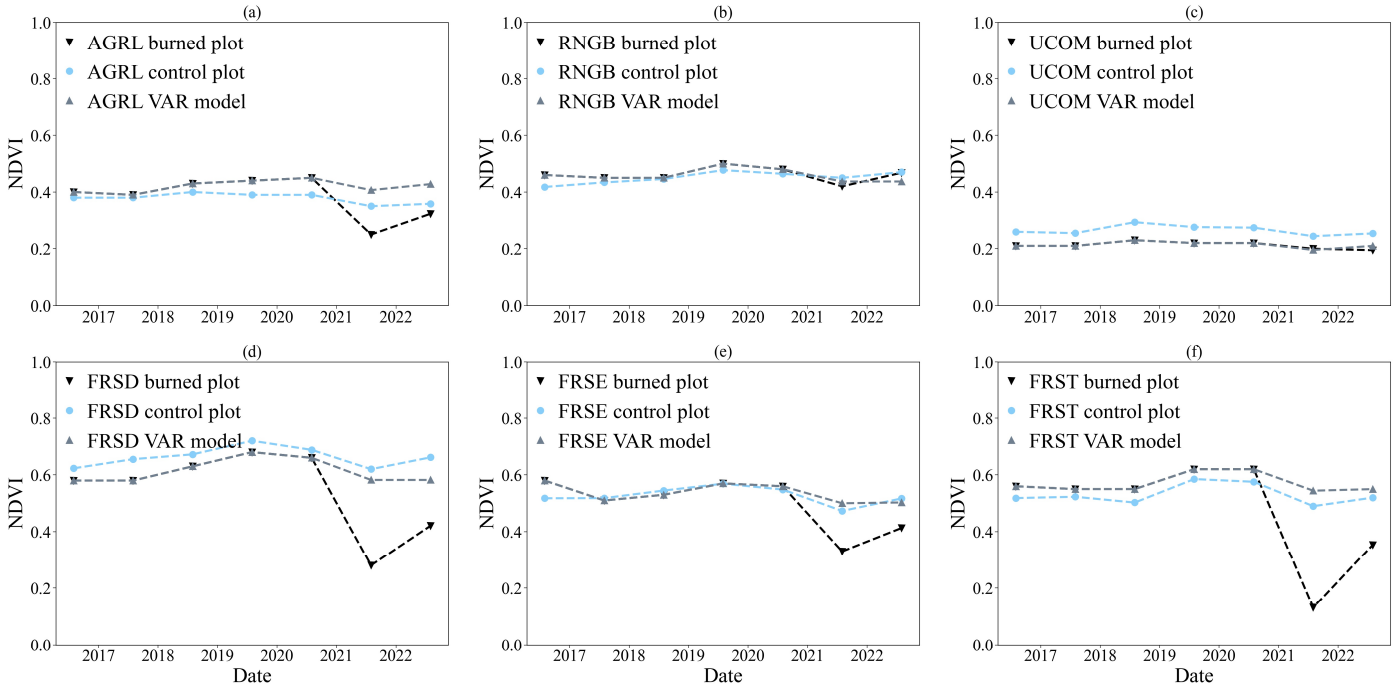

Figure 4. Mean $NDVI$ for the burned and control plots and VAR modeling results from August 2021 to August 2022. (**a**) AGRL, agriculture. (**b**) RNGB, shrubland. (**c**) UCOM, transportation/green areas. (**d**) FRSD, deciduous forest. (**e**) FRSE, evergreen forest. (**f**) FRST, mixed forest.

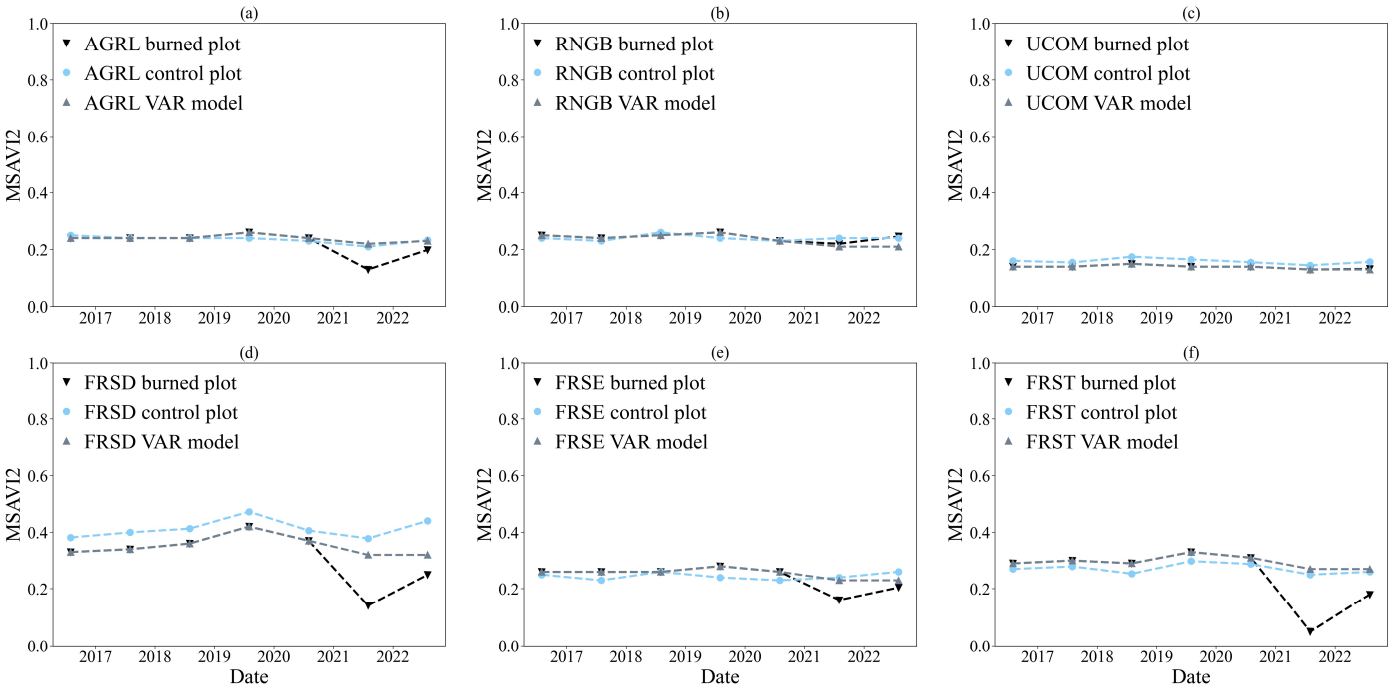

Figure 5. Mean $MSAVI_2$ for the burned and control plots and VAR modeling results for August 2016–August 2022. (**a**) AGRL, agriculture. (**b**) RNGB, shrubland. (**c**) UCOM, transportation/green areas. (**d**) FRSD, deciduous forest. (**e**) FRSE, evergreen forest. (**f**) FRST, mixed forest.

Table 2. Mean $NDVI$ and $MSAVI_2$ differences for each land use category between burned and control plots. $\%\Delta NDVI = NDVI_{burned} - NDVI_{control}$ and $\%\Delta MSAVI_2 = MSAVI2_{burned} - MSAVI2_{control}$.

Months	AGRL %difference		RNGB %difference		UCOM %difference		FRSD %difference		FRSE %difference		FRST %difference	
	NDVI	$MSAVI_2$	*NDVI*	$MSAVI_2$	*NDVI*	$MSAVI_2$	*NDVI*	$MSAVI_2$	*NDVI*	$MSAVI_2$	*NDVI*	$MSAVI_2$
16 August	5.26	−4.00	10.10	4.17	−19.17	−12.85	−6.92	−13.52	12.00	4.00	8.00	7.44
17 August	2.63	0.00	3.73	4.35	−17.64	−9.54	−11.49	−14.89	−1.62	13.04	5.15	7.52
18 August	7.50	0.00	0.95	−3.85	−21.66	−14.26	−6.28	−12.75	−2.73	0.00	9.42	14.45
19 August	12.82	8.33	4.80	8.33	−20.38	−15.28	−5.55	−11.12	0.17	16.67	5.94	10.78
20 August	15.38	4.35	3.41	0.00	−19.82	−10.04	−4.08	−8.86	2.10	13.04	7.68	7.75
21 August	−28.57	−38.10	−6.67	−8.33	−18.12	−10.20	−54.85	−62.97	−30.26	−33.33	−73.47	−80.00
22 August	−9.81	−14.65	−0.44	2.37	−23.27	−15.76	−36.39	−43.33	−20.13	−21.41	−32.14	−30.98

3.1.3. Burn Severity and Vegetation Response

The burn severity map (Figure 1) was compared with vegetation data for the pre-fire and post-fire periods to investigate their relationship. Figures 6 and 7 show the mean $NDVI$ and $MSAVI_2$ of the burned area land use categories by burn severity class. The post-fire images showed that both vegetation indices declined sharply for the moderately and highly burned classes. In particular, for the mixed forest category (FRST), which had the highest burned percentage (i.e., 65.4%), the mean $NDVI$ decreased by 0.48, from 0.59 in July 2021 to 0.11 in August 2021, and the mean $MSAVI_2$ decreased by 0.27, from 0.31 in July 2021 to 0.04 in August 2021. Regarding the $NDVI$, in the same land use category, the areas of moderate-severity burn decreased by 0.38, and the areas of low-severity burn decreased by 0.24 over the same period. For the $MSAVI_2$, the areas of moderate-severity burn decreased by 0.22, and the areas of low-severity burn decreased by 0.15, respectively. One year after the wildfire, the greatest increase in the $NDVI$ and $MSAVI_2$ was observed in the moderately and highly burned areas, demonstrating that highly burned areas showed faster recovery. In contrast, the increases in the $NDVI$ and $MSAVI_2$ for the unburned and low-severity classes were more moderate.

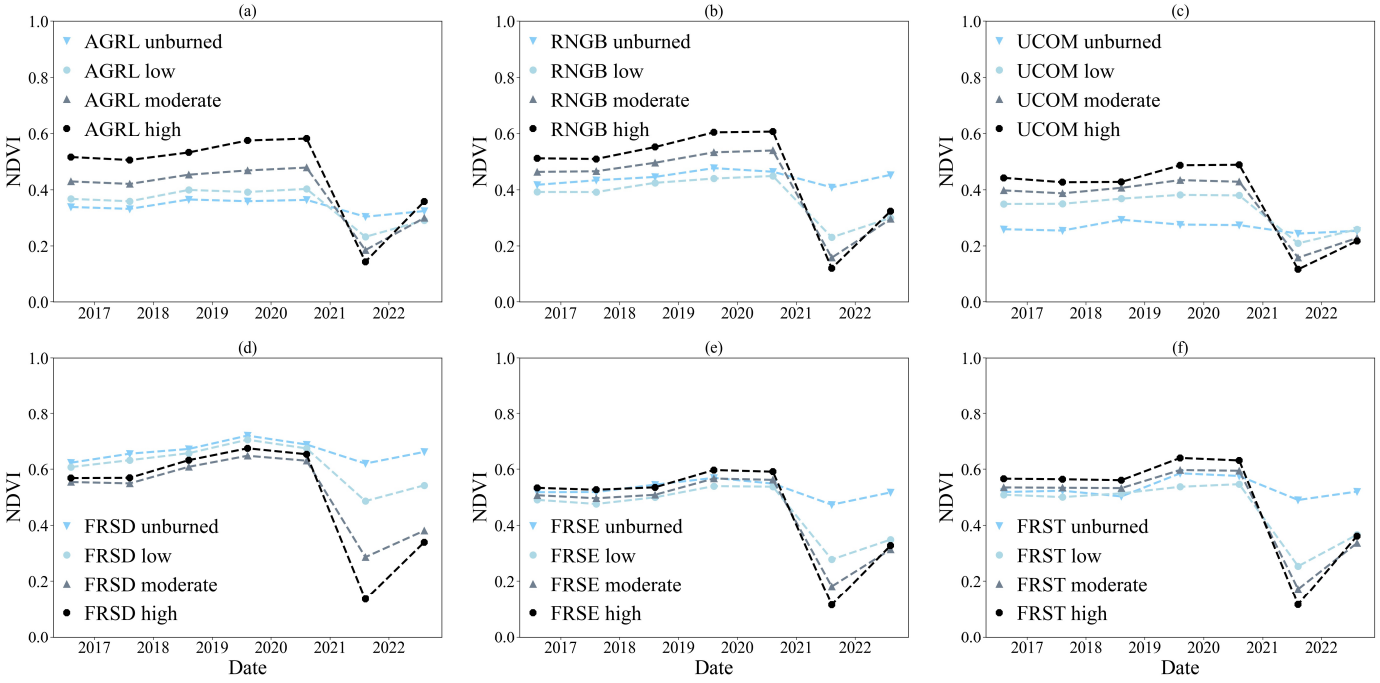

Figure 6. Mean $NDVI$ by burn severity class, August 2016–August 2022. (**a**) AGRL, agriculture. (**b**) RNGB, shrubland. (**c**) UCOM, transportation/green areas. (**d**) FRSD, deciduous forest. (**e**) FRSE, evergreen forest. (**f**) FRST, mixed forest. All classes demonstrated consistently positive post-fire $NDVI$ gains in the first post-fire year.

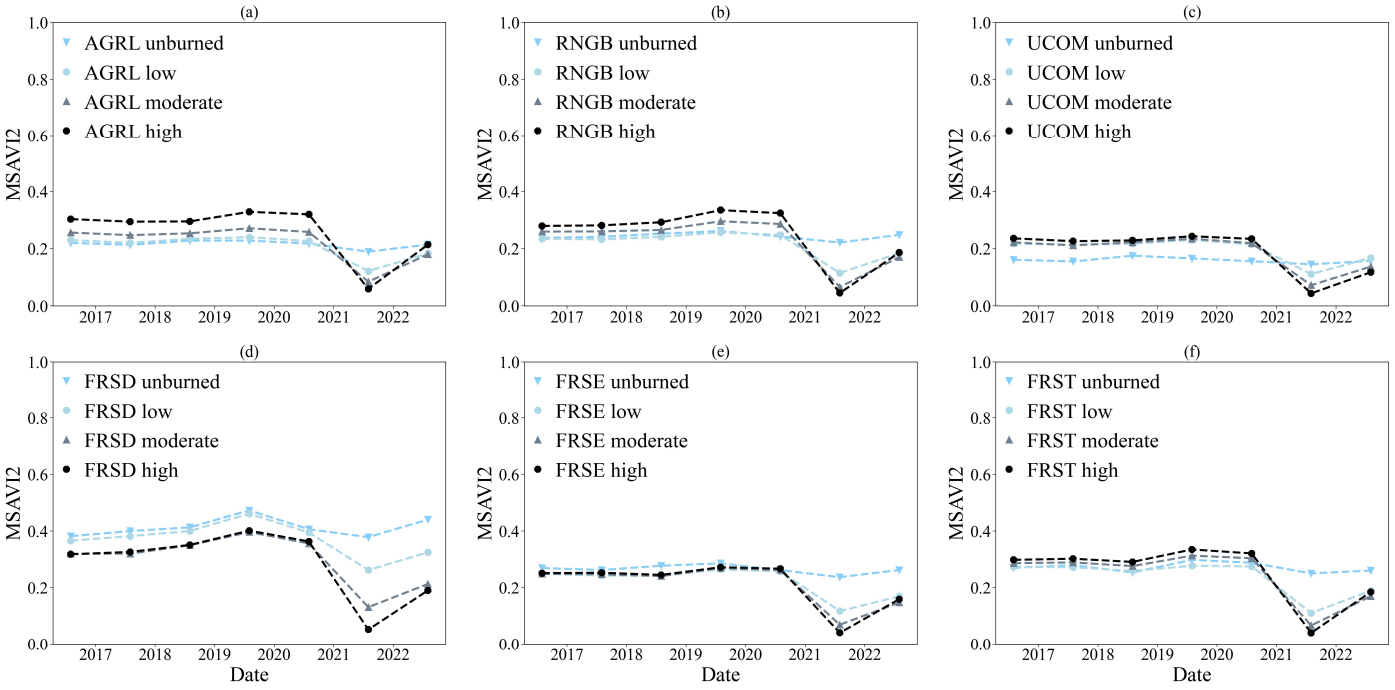

Figure 7. Mean $MSAVI_2$ by burn severity class, August 2016–August 2022. (**a**) AGRL, agriculture. (**b**) RNGB, shrubland. (**c**) UCOM, transportation/green areas. (**d**) FRSD, deciduous forest. (**e**) FRSE, evergreen forest. (**f**) FRST, mixed forest. All classes demonstrated consistently positive post-fire $MSAVI_2$ gains in the first post-fire year.

3.2. Post-Fire Assessment of Hydrological Response

3.2.1. Model Performance

The pre-fire scenario was calibrated from January 2018 to December 2018 and validated from January 2019 to March 2020. The evaluation was performed for both daily and hourly time steps, and the annual precipitation and discharge statistics were used to examine biases in discharge patterns. The simulation period represented both wet and dry periods, with 2018 having an annual precipitation of 566 mm, and 2019 receiving 735 mm. The mean and standard deviation of discharge for 2018 were 1.25 and 0.46, respectively, and for 2019, they were 1.42 and 0.74.

Table 3 shows the model evaluation metrics at both the daily and hourly time steps, and indicates reasonable performance [82]. However, the daily model exceeded the hourly model for both calibration and validation periods (e.g., sub-daily model: $NSE_{calibration}$ = 0.49 and $NSE_{validation}$ = 0.6, daily model: $NSE_{calibration}$ = 0.79 and $NSE_{validation}$ = 0.86). Additionally, the daily model exhibited minor modeling uncertainties with a *p*-factor of 0.79 and an R-factor of 1.58 (compared to 0.83 and 1.71, respectively, for the sub-daily model). Therefore, using the calibrated parameters from the pre-fire model is acceptable, as the satisfactory model performance demonstrates reasonable accuracy in predicting discharge.

Table 3. Model performance statistics of the pre-fire model at daily and hourly temporal scales.

Time-Step	Period	*p*-Factor	r-Factor	R^2	NSE	PBIAS (%)
Daily	Calibration	0.74	1.41	0.84	0.79	6.4
	Validation	0.79	1.58	0.87	0.86	4.2
Sub-Daily	Calibration	0.72	1.33	0.53	0.49	16.9
	Validation	0.83	1.71	0.63	0.6	11.7

The post-fire scenario was calibrated using the calibrated values of the pre-fire scenario for the unburned areas and adjusting the parameter values only for the burned areas

of the catchment. The calibrated parameters representing surface runoff, groundwater, and channel routing for the burned and unburned areas are presented in Table 4. The two scenarios (i.e., pre-fire and post-fire) were applied for the entire simulation period (1 January 2018 to 31 December 2022) to equally compare the impact of post-fire land use and soil properties changes in the hydrological balance. Furthermore, considering that the post-fire period from January 2022 to December 2022 displayed lower annual precipitation (365.2 mm) (i.e., a drier year than 2018 and 2019), and that the pre-fire scenario's calibrated values incorporated both dry and wet years, the predictive ability of the post-fire scenario is supported.

Table 4. Calibrated parameters used in the pre-fire and post-fire scenarios. The method "r" indicates that the parameter value is to be multiplied by (1 + a given value), the method "v" indicates that the parameter value is going to be replaced, and the method "a" indicates that the parameter is to be added to a given value [81].

Process	Parameter	Description	Method	Daily	Sub-Daily
				Range	Range
Surface runoff	CN2	Curve number	r (relative)	(−0.04, 0.1)	(−0.002, 0.1)
Groundwater	ALPHA_BF	Baseflow alpha factor	v (replace)	(0.05, 0.69)	(0.5, 1)
	GW_DELAY	Groundwater delay	a (absolute)	(10, 95)	(10, 80)
	RCHRG_DP	Deep aquifer percolation fraction	v (replace)	(0, 0.5)	(0.11, 0.4)
	REVAPMN	Threshold depth of water for "revap" to occur	v (replace)	(990, 1800)	(800, 1800)
	GW_REVAP	Groundwater "revap" coefficient	v (replace)	(0.02, 0.2)	(0.06, 0.21)
	GWQMN	Threshold depth of water for return flow to occur	v (replace)	(100, 500)	(150, 500)
Lateral flow	HRU_SLP	Average slope steepness	r (relative)	(−0.01, 3)	(0.2, 2.3)
Channel	SLSUBBSN	Average slope length	r (relative)	(−0.1, 0.2)	(−0.6, 0.2)
Soil	USLE_C	Crop vegetation factor	v (replace)	(0.01, 0.2)	(0.01, 0.2)
	CHTMX	Maximum canopy storage	r (relative)	(−0.6, 0.1)	(−0.6, 0.1)
	USLE_K	Soil erodibility factor	v (replace)	(0.01, 0.2)	(0.01, 0.2)
	SOL_BD	Moist bulk density of the soil layer	r (relative)	(−0.1, 0.3)	(−0.1, 0.3)
	SOL_AWC	Soil available water storage capacity	r (relative)	(−0.03, 0.03)	(−0.03, 0.03)
	SOL_K	Saturated hydraulic conductivity	r (relative)	(−0.2, 0.8)	(−0.2, 0.8)
	SOL_CBN	Organic carbon content	r (relative)	(−0.02, 0.02)	(−0.02, 0.02)
	ESCO	Soil evaporation compensation coefficient	v (replace)	(0.5, 0.95)	(0.5, 0.95)

3.2.2. Hydrological Response

The daily and hourly hydrographs during the pre-fire and post-fire periods are depicted in Figures 8 and 9. In general, in the pre-fire period, the models captured most of the seasonality and peak discharge of the observed values, indicating good agreement between the observed and simulated values (Figures 8a and 9a). In the post-fire period, the daily maximum simulated discharge increased from 10.5 m^3/s to 35.2 m^3/s, indicating a considerable increase in runoff generation after the fire event. The maximum daily rainfall depths for these periods were 67.60 mm and 101.40 mm, respectively. Figures 8a and 9a show that similar rainfall depths resulted in higher peak discharges in the post-fire period. Higher peak discharges were observed in the entire post-fire period. Furthermore, the flow duration curves (FDCs) for the pre-fire and post-fire scenarios at a daily and hourly time step for the entire simulation period were also compared (Figures 8b and 9b). Both scenarios had similar middle and lower parts of the flow duration curves (i.e., baseflow). The upper portion of the curve (e.g., high-flow events) for the post-fire scenario was characterized by steeper slopes and higher peaks. This observation indicates higher variability in flow regimes and a more rapid response to precipitation events after the fire.

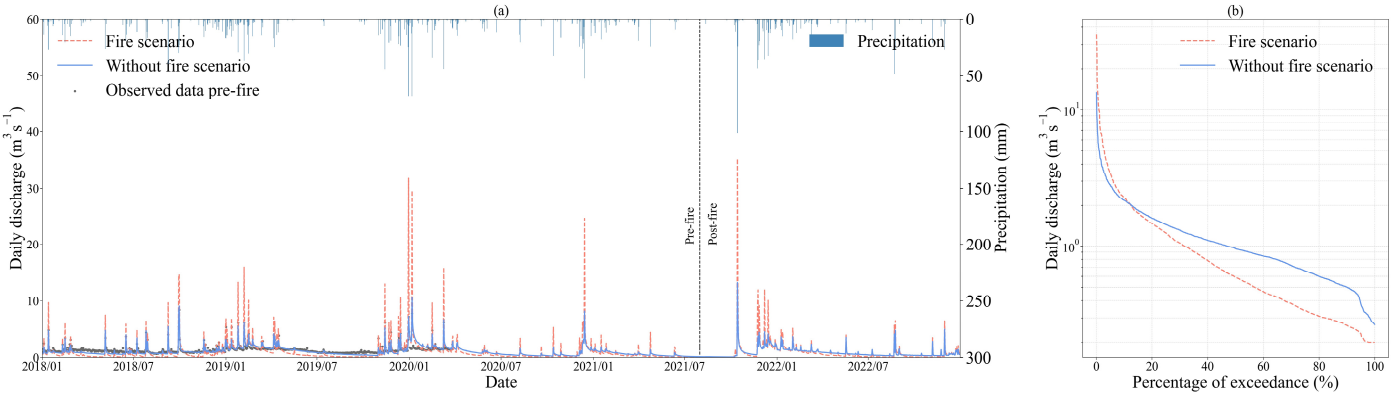

Figure 8. Simulated daily discharge results (**a**) and flow duration curves (**b**) (m^3 s^{-1}) during the pre-fire and post-fire scenarios.

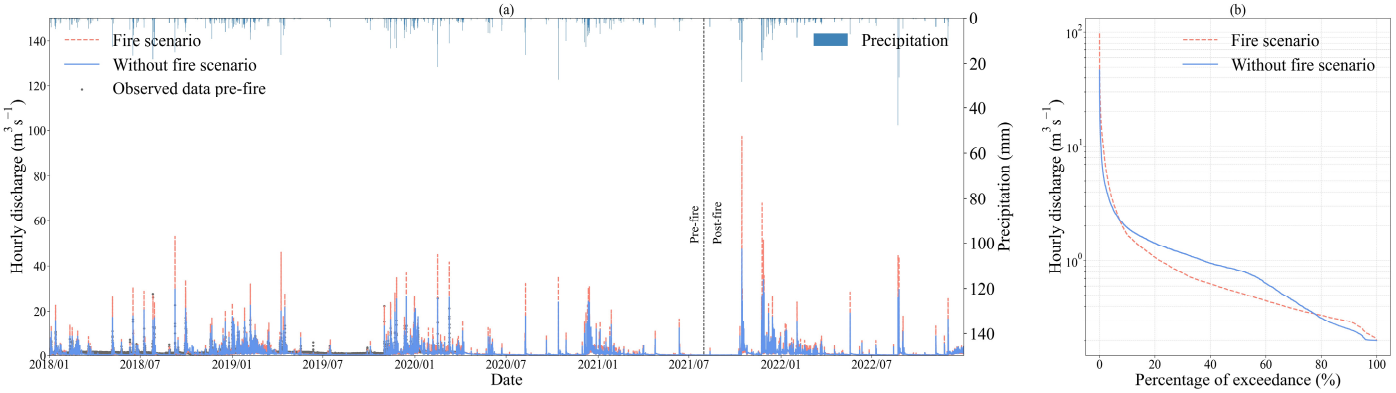

Figure 9. Simulated hourly discharge results (**a**) and flow duration curves (**b**) (m^3 s^{-1}) during the pre-fire and post-fire scenarios.

In addition, the maximum hourly discharges (m^3/s) were compared with the maximum hourly rainfall intensity (mm/h) for rainfall events before and after the fire, as shown in Figure 10. The red and blue dots represent the post-fire and pre-fire periods, respectively. The size of the circles is according to the peak discharge for the pre- and post-fire conditions. The maximum hourly discharge during the pre-fire period was 26.1 m^3/s, whereas during the post-fire period, it was 97.4 m^3/s. At the same time, the maximum hourly rainfall intensity was 12.0 mm/h for the pre-fire period and 28.0 mm/h for the post-fire period. For instance, as shown in Figure 10, the pre-fire maximum hourly rainfall intensity of 13.20 mm/h led to a 17.30 m^3/s maximum hourly discharge. In the same figure, it can be seen that in the post-fire periods, the same maximum hourly rainfall intensity of 13.80 mm/h led to a 25.50 m^3/s maximum hourly discharge. It was similarly observed that there were higher peak discharges for the post-fire period in comparison to the pre-fire period for the same rainfall intensities. Overall, these differences between the two scenarios indicate high discharge for a short time period.

Furthermore, to analyze the interactions between the major hydrological components of the pre-fire and post-fire scenarios, their monthly values were plotted against the precipitation depth (Figures 11 and 12). Similar patterns were observed for both conditions. Wildfires can reduce vegetation and ground cover, resulting in a reduction in actual evapotranspiration. Actual evapotranspiration was lower by about 9.6% when the impact of the fire was considered. The lower actual evapotranspiration and the loss of the topsoil organic matters led to increased water yield. Indeed, the water yield, percolation, and surface runoff were generally higher in the post-fire conditions. In particular, in the daily model, the surface runoff was higher by about 32.8%, and percolation was higher by 58.1% in the post-fire scenario. Actual evapotranspiration was lower by about 9.6% when the impact

of the fire was considered. It was also noticed that the differences in the hydrological components between the two scenarios were more pronounced during the wet season, especially for high precipitation depths (similarly to Figures 9 and 10). During the dry season, the hydrological components were similar for both scenarios. Notably, additional data are required to investigate the runoff response during the dry and wet years.

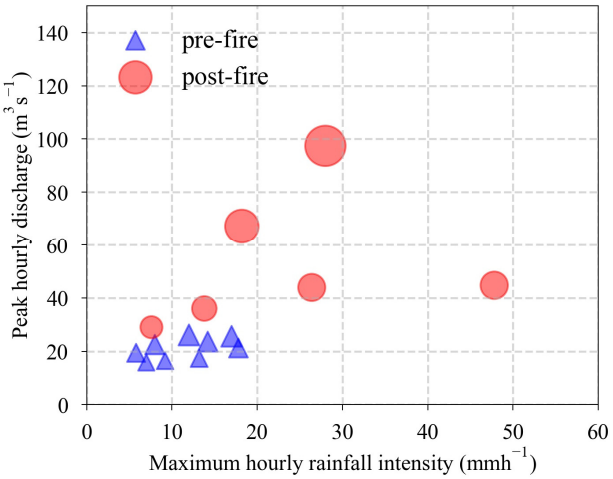

Figure 10. Maximum hourly discharge (m^3s^{-1}) of the rainfall events that occurred in the pre-fire and post-fire periods compared to maximum hourly rainfall intensity (mmh^{-1}). The size of the circles is according to the peak discharge for the pre- and post-fire conditions.

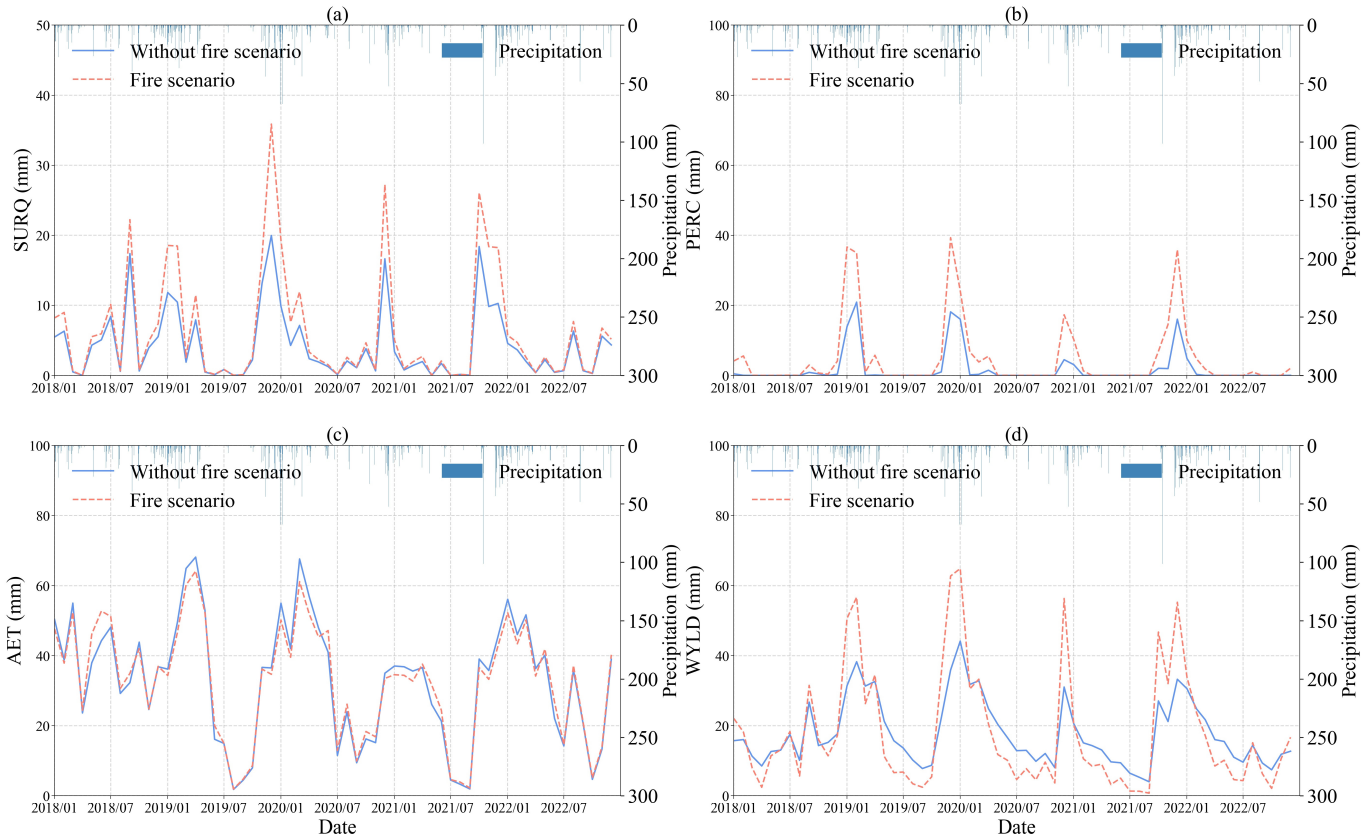

Figure 11. Monthly values of the major hydrological components of the daily (**a**–**d**) model during the pre-fire and post-fire scenarios. SURQ: surface runoff (mm), PERC: percolation (mm), AET: actual evapotranspiration (mm), and WYLD: water yield (mm).

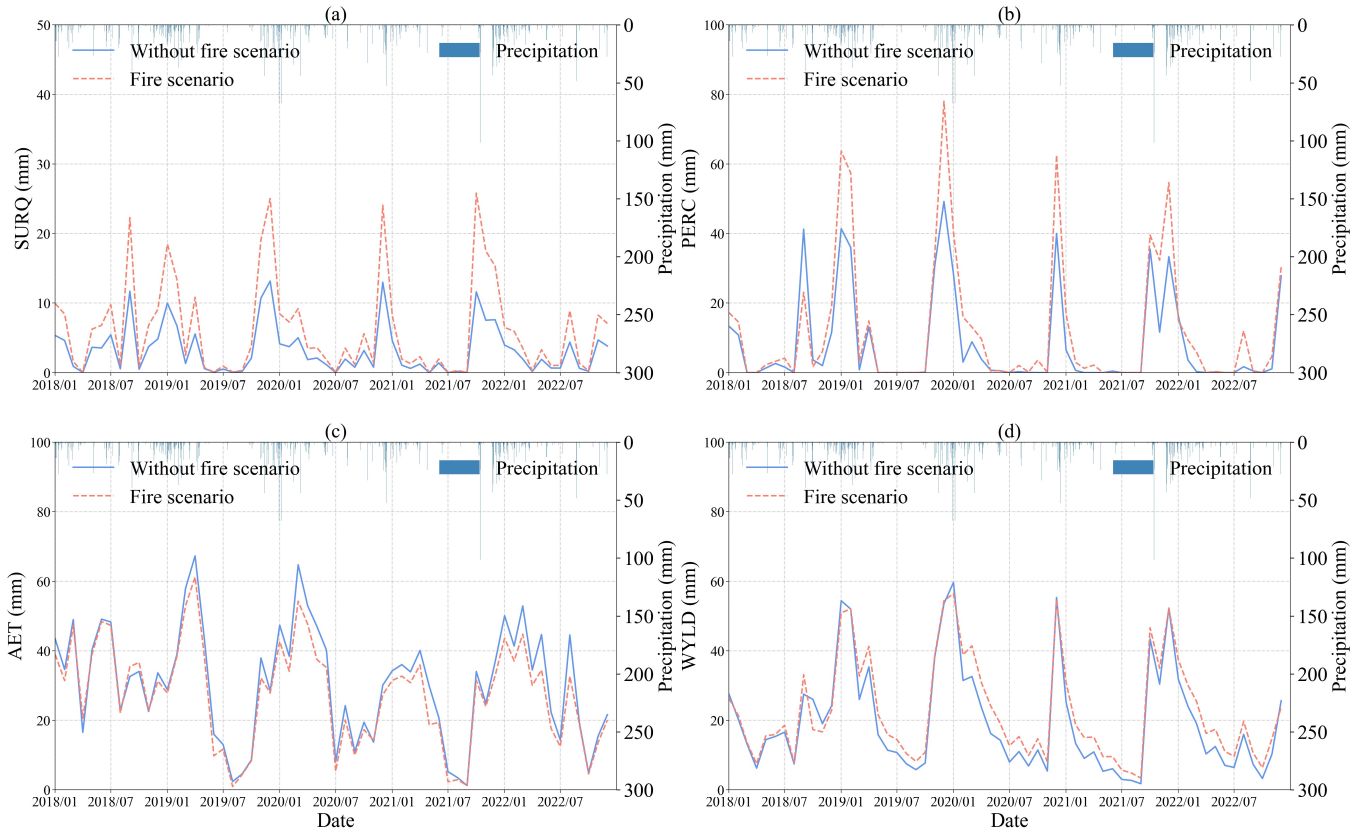

Figure 12. Monthly values of the major hydrological components of hourly (**a**–**d**) model during the pre-fire and post-fire scenarios. SURQ: surface runoff (mm), PERC: percolation (mm), AET: actual evapotranspiration (mm), and WYLD: water yield (mm).

4. Discussion

4.1. Post-Fire Impacts on the Vegetation Response

In this study, remote sensing techniques were used to assess the impact of the 2021 wildfire in the Kifisos experimental subbasin. The burn severity map created using the $dNBR$ index showed that the burned area mainly consisted of highly and moderately burned areas, while the low-burn-severity class and unburned areas accounted for a relatively small percentage (Figure 1). The land use categories most affected by the fire were the mixed forest, deciduous forest, evergreen forest, and shrubland. The agricultural areas had moderately burned areas, and the artificial areas included mainly low-burn-severity areas. Similar results have been observed by Falaras et al. [54], who investigated the influence of the 2021 wildfires in the Attica region on soil erosion using remote sensing, GIS-based techniques, and the revised universal soil loss equation (RUSLE) model. According to their findings, the fire mostly affected forestry areas consisting of broad-leaved, sclerophyllous, and mixed vegetation. The forests exhibited moderate to high burn severity, while agricultural areas showed moderate to low burn severity. In addition, higher erosion risks were noticed in the burned forest areas. These observations were also evident from the distribution of high-burn-severity areas across different subbasins. Subbasins that contained the aforementioned land use categories (ID = 3, 1, 20) presented the highest percentage of high burn severity. This information is significant for prioritizing land management and post-fire recovery measures (e.g., reforestation, soil stabilization, erosion control), as it identifies the most affected areas that require immediate attention.

Furthermore, vegetation recovery was examined by analyzing the $NDVI$ and $MSAVI_2$. A Vector Autoregressive (VAR) model was developed to analyze the time series data without the impact of fire and to forecast future values. The values extracted from the forecasting model and the unburned/minimally affected subbasins were used as control values to

assess the vegetation dynamics. The results showed that one-year post-fire $NDVI_{burned}$ and $MSAVI_{2burned}$ values were mainly below those of the unburned control plots. The vegetation indices of the burned plots declined substantially for the forest—deciduous (FRSD), forest—evergreen (FRSE), and forest—mixed categories (FRST), and they still lagged behind the control plots one year post-fire. Only the categories agriculture (AGRL), shrubland (RNGB), and transportation/green areas (UCOM) showed rapid recovery.

These results indicate that vegetation recovery varies depending on the land use category, with some categories recovering faster than others [2]. However, the different recovery rates across these land use categories could also be attributed to the anthropogenic impact on the vegetation indices, which are correlated with grazing and crop cultivation [14]. Vegetation recovery rates in warmer climates, such as Mediterranean areas, are typically more moderate [86]. It should be noted that, although the $NDVI$ is responsive to variations in vegetation density and fire heterogeneity [18], both vegetation indices followed similar trends for all land use categories (Figures 4 and 5), suggesting gradual recovery to pre-fire conditions. Moreover, the use of the VAR model in this study provides an important tool for predicting vegetation dynamics and quantifying the impacts of disturbances on ecosystems. The time series derived from the control plots showed similar patterns to those derived from the forecasting model, validating the model's predictive ability and its usefulness in quantifying vegetation response.

Finally, the burn severity map and vegetation data were combined to evaluate the correlation between vegetation recovery and burn severity one year after the fire. The results showed that the mean $NDVI$ and $MSAVI_2$ values of the burned area decreased significantly for the moderately and highly burned classes (Figures 6 and 7). One year after the fire, the highly and moderately burned areas showed the highest increase in the $NDVI$ and $MSAVI_2$, while the unburned and low-severity areas displayed a moderate increase, indicating the influence of burn severity on vegetation recovery. The different behaviors between the burn severity classes demonstrate the complexities of post-fire vegetation dynamics. Lee and Chow [34] reported that highly burned areas showed the highest gains in the $NDVI$ during the first two years post-fire; however, they exhibited a net decline in the third year. Similarly, regeneration has also been observed in highly burned areas during the initial post-fire years [14,25,26]. However, higher rates of regeneration in the long term were observed in low-severity areas, indicating a spatial heterogeneity in vegetation response influenced by localized factors. These results highlight the complex relationship between burn severity and vegetation response [13,27] and emphasize the importance of monitoring vegetation dynamics over time to assess the long-term effects of fires on ecosystems.

The outcomes suggest that remote sensing techniques can be used as a cost-effective post-fire assessment and rehabilitation measure. The analysis of burn severity and vegetation response provides insights into identifying rehabilitating areas with slow or unsuitable post-fire vegetation recovery [87]. Also, monitoring the post-fire trends in these areas helps local planners determine if the ecosystems are returning to the pre-fire conditions and whether rehabilitating programs are effective [26]. It is worth mentioning that this is a preliminary study, and it is too early to predict the recovery period, as only one year has passed. In addition, the inadequate resolution of satellite data, the choice of monthly temporal resolution, and observational errors may prevent the capture of fine-scale variability in land use and topography, which could introduce bias into the model results. For future research, additional analysis supported by field observations, burn severity maps, and continued vegetation index analysis is necessary to investigate whether the increase in the highly and moderately burned areas is temporary or a lasting trend. This approach can help identify the best locations, timing, and methods for implementing restoration treatments and support efforts to restore vegetation to its pre-fire condition.

4.2. Post-Fire Impacts on the Hydrological Response

The SWAT model was applied to investigate the effects of fire on the water balance of a Mediterranean peri-urban catchment vulnerable to natural hazards. The main objective was to analyze the interactions between the major hydrological components and to provide a methodology for integrating burn severity into SWAT modeling. The SWAT model performed satisfactorily under pre-fire conditions at both daily and hourly time scales, as indicated by the statistical analysis (Table 3). Better results were observed with the daily interval compared to the hourly calibration and validation. These differences can be attributed to the different runoff estimation methods employed by the two models [88]. The daily model used the CN method, while the hourly model used the GAML method for surface runoff estimation. The GAML method requires detailed soil data and high-resolution precipitation information. Additionally, it assumes that the soil profile is homogeneous and that the previous soil moisture is uniformly distributed throughout the profile [89]. Therefore, the method's efficiency could be affected by uncertainties in precipitation data resolution, soil heterogeneity, catchment size, and difficulties in parameterization [90–92]. Overall, the satisfactory model performance of the pre-fire scenario indicates that the calibrated pre-fire model can be used as a suitable baseline for predicting post-fire runoff.

Model calibration and validation could not be performed for post-fire conditions since no discharge data were available, and only one hydrological year has passed since the fire event. In addition, difficulties in installing and maintaining monitoring stations and instruments in burned catchments during post-fire conditions make obtaining observed discharge data challenging. The limited availability of data emphasizes the importance of collecting such information for the scientific community and local communities to mitigate potential post-fire impacts [4,93].

The post-fire scenario was calibrated using the pre-fire model's calibrated values for the areas unaffected by the fire (Table 4). In order to ensure an equal evaluation of the effects of post-fire changes in land use and soil properties on the hydrological balance, both the pre-fire and post-fire versions of the model were applied for the entire simulation period (1 January 2028 to 31 December 2022). An increase in surface runoff was generally observed at the subbasin scale following the occurrence of fire (Figures 8 and 9). The hydrographs and the flow duration curves of the two models indicated higher peak discharges during the post-fire period. Previous studies on flow duration curves for pre- and post-fire scenarios have also found an increase in discharge due to the fire's impact [41,94]. In addition, this increase was evident from the analysis of maximum hourly discharges in comparison to the maximum hourly rainfall intensity (mm/h) of rainfall events (Figure 10). Higher peak discharges were observed during the same rainfall intensities for the post-fire period. Similar results were found in previous studies that noted an enhancement of the hydrological response during the post-fire period. A case study in the Zêzere River catchment [4] and a case study in the Macieira de Alcôba mountain catchment [49] in Portugal also indicated increased surface runoff and sediment concentration at the subbasin level after the fire event.

Severe destruction of vegetation cover due to a high percentage of burn severity can lead to reduced catchment evapotranspiration rates during the early post-fire period, while differences in soil attributes can affect runoff generation mechanisms [3,6,95,96]. In this study, in addition to surface runoff, water yield and percolation were also higher under post-fire conditions, whereas actual evapotranspiration was lower (Figures 11 and 12). These results align with previous research studies which mentioned decreases in evapotranspiration and increases in surface runoff due to the post-fire changes in land use cover and soil characteristics [10,11,41,50]. For example, Zhou et al. [10], in a study of a bushfire in southeast Australia, concluded that reduced evapotranspiration and soil infiltration led to increased streamflow. Similarly, Havel et al. [41] reported higher surface runoff and reduced subsurface flow. Poon and Kinoshita [11] and Soulis et al. [50] observed that the loss of xerophytic bushes and trees with deep roots, replaced by grasslands, resulted in

an overall decrease in evapotranspiration after the fire. Additionally, Pereira et al. [3] and Wijesekara et al. [97] reported increased runoff peaks during wet periods and decreased runoff during dry periods.

The limited research on post-fire vegetation recovery and hydrological responses in Mediterranean regions highlights the important relationship between ecological and hydrological processes in such fire-vulnerable ecosystems. A case study in Southern California (characterized by a Mediterranean climate, Köppen Csa; hot, dry summers and cool, wet winters) evaluated post-fire hydrological and vegetation recovery using satellite data and local rainfall–runoff data, revealing how vegetation types and pre-fire conditions shape recovery patterns [98]. The results showed that post-fire changes in vegetation influence hydrological components, including an increase in surface runoff and a decrease in actual evapotranspiration. Similarly, a study in central Chile showed how fire severity combined with drought stressors affects forest recovery, indicating the importance of managing these dual stressors for ecosystem resilience [99]. They concluded that although Mediterranean ecosystems are characterized by their resilience to wildfires, drought conditions and fire severity can create challenges for vegetation recovery. Both findings highlight the need for integrating post-fire vegetation and hydrological monitoring to guide management practices and enhance ecosystem resilience.

However, the increase in peak discharges can be attributed to a variety of factors, including differences in soil hydraulic conductivity, rapid surface, and channel flow due to vegetation destruction, antecedent conditions, and increased initial soil moisture resulting from evapotranspiration reduction, grazing, and logging activities [36,37]. The discrepancy between different resolutions of input data (i.e., soil, land use, elevation, climate, and remote sensing data) could introduce uncertainties in SWAT simulation results by affecting the spatial distribution of properties, model calibration, temporal dynamics, and model sensitivity [100–102]. The use of input data with varying resolutions could potentially affect the SWAT model's ability to capture rapid changes in discharge following the fire event. Identifying the mechanisms behind this phenomenon poses a significant challenge that requires in-depth research. Such investigations may provide a more comprehensive understanding of the hydrological response recovery process, the duration of the post-fire recovery period, and the efficacy of various post-fire mitigation actions. Furthermore, improving SWAT model calibration by incorporating discharge and soil moisture data into a combined objective function, along with updated meteorological data and the integration of different vegetation scenarios, is essential. This methodology can be applied to catchments with different hydrological and geomorphological characteristics, enabling extended future research into rainfall patterns and soil moisture conditions.

5. Conclusions

This study investigated the connection between burn severity and the vegetation and hydrological response of a Mediterranean peri-urban system of high environmental and socio-economic importance affected by a fire, using remote sensing data and hydrological modeling. $NDVI$ and $MSAVI_2$ time series extracted from unburned control plots and Vector Autoregression (VAR) model control plots provided a reliable and valuable tool to evaluate the system's vegetation regrowth after the fire. The SWAT model and detailed hydro-meteorological data were also used to examine the hydrological response after the fire. The main outcomes are summarized below:

- During the first post-fire year, vegetation showed slight recovery in highly burned areas. The mean $NDVI$ and $MSAVI_2$ within the burned area were still lower than those within the control plots. The analysis of the vegetation indices and burn severity showed the different responses of each burn severity class regarding post-fire vegetation dynamics. The most significant increases in the $NDVI$ and $MSAVI_2$ were observed in high- and moderate-burn-severity areas. The high-burn-severity areas were associated with densely vegetated areas, emphasizing the influence of pre-fire vegetation attributes on burn severity.

- The SWAT model was calibrated only for pre-fire conditions, as discharge data were unavailable after the fire. Despite limitations due to the absence of data, the SWAT model proved to be an essential tool for investigating the effect of fire on the hydrological components. In the post-fire conditions, an increase in surface runoff, water yield, and percolation was observed, as well as a decrease in actual evapotranspiration. The simulated hydrograph displayed higher peak discharges, particularly during the wet period.
- The changes in post-fire land use and soil attributes were identified as the primary drivers of the catchment's water balance. However, identifying the mechanisms controlling surface runoff remains challenging, as other factors could also be involved.

This study enhances the existing literature by investigating the vegetation and hydrological response of an experimental catchment to assess the initial effects of a fire. There is limited research on the interrelationships of vegetation recovery, hydrological response, and burn severity. The preliminary results contribute to the understanding of Mediterranean systems dynamics and highlight the complementary nature of vegetation recovery analysis and hydrological modeling in understanding post-fire dynamics. Assessing burn severity can also provide valuable insights for land management practices. It is important to acknowledge that uncertainties in model outcomes may arise from various factors, including data limitations, observational errors in input data, complexities in spatial and temporal scales, and inaccuracies in model structure.

Author Contributions: Conceptualization, E.K., N.M., E.B., V.A. and A.K.; methodology, E.K., N.M., E.B., V.A. and A.K.; validation, E.K., N.M., E.B., V.A. and A.K; formal analysis, E.K., N.M., E.B., V.A. and A.K; investigation, E.K., N.M., E.B., V.A. and A.K; resources, E.K., N.M., E.B., V.A. and A.K; data curation, E.K., N.M., E.B., V.A. and A.K; writing—original draft preparation, E.K.; writing—review and editing, E.K., N.M., E.B., V.A. and A.K; visualization, E.K.; supervision, A.K., N.M. and E.B.; project administration, A.K.; funding acquisition, A.K. All authors have read and agreed to the published version of the manuscript.

Funding: This research work was supported by the Hellenic Foundation for Research and Innovation (HFRI) under the HFRI PhD Fellowship grant (Fellowship Number: 1586).

Data Availability Statement: The SWAT model is available at https://doi.org/10.1111/j.1752-1688.1998.tb05961.x [74]. The digital elevation model (DEM) data and the Landsat datasets were downloaded from https://earthexplorer.usgs.gov/ (accessed on 5 December 2020) [61]. The land use data were downloaded from https://land.copernicus.eu/ (accessed on15 December 2020) [59]. The soil data were downloaded from http://www.fao.org/ (accessed on 15 December 2020) [58]. The weather data were downloaded from https://www.meteo.gr/ (accessed on 20 December 2020) [57]. The discharge data were downloaded from https://openhi.net/ (accessed on 10 December 2020) [62]. Landsat algorithms are available at https://developers.google.com/earth-engine/guides/landsat (accessed on 12 December 2024) [103].

Acknowledgments: The authors are grateful to Karim Abbaspour from the Swiss Federal Institute of Aquatic Science and Technology (Eawag) for providing the hourly SWAT-CUP package. The authors would also like to thank the anonymous reviewers for their comments and suggestions.

Conflicts of Interest: The authors declare no conflicts of interest. The funders had no role in the design of the study; in the collection, analyses, or interpretation of data; in the writing of the manuscript; or in the decision to publish the results.

References

1. Chuvieco, E.; Aguado, I.; Salas, J.; García, M.; Yebra, M.; Oliva, P. Satellite Remote Sensing Contributions to Wildland Fire Science and Management. *Curr. For. Rep.* **2020**, *6*, 81–96. [CrossRef]
2. Yang, J.; Pan, S.; Dangal, S.; Zhang, B.; Wang, S.; Tian, H. Continental-scale quantification of post-fire vegetation greenness recovery in temperate and boreal North America. *Remote Sens. Environ.* **2017**, *199*, 277–290. [CrossRef]
3. Pereira, M.G.; Fernandes, L.S.; Carvalho, S.; Santos, R.B.; Caramelo, L.; Alencoão, A. Modelling the impacts of wildfires on runoff at the river basin ecological scale in a changing Mediterranean environment. *Environ. Earth Sci.* **2016**, *75*, 392. [CrossRef]

4. Basso, M.; Vieira, D.C.S.; Ramos, T.B.; Mateus, M. Assessing the adequacy of SWAT model to simulate postfire effects on the watershed hydrological regime and water quality. *Land Degrad. Dev.* **2020**, *31*, 619–631. [CrossRef]
5. Moody, J.A.; Shakesby, R.A.; Robichaud, P.R.; Cannon, S.H.; Martin, D.A. Current research issues related to post-wildfire runoff and erosion processes. *Earth-Sci. Rev.* **2013**, *122*, 10–37. [CrossRef]
6. Ebel, B.A.; Moody, J.A.; Martin, D.A. Post-fire temporal trends in soil-physical and -hydraulic properties and simulated runoff generation: Insights from different burn severities in the 2013 Black Forest Fire, CO, USA. *Sci. Total Environ.* **2022**, *802*, 149847. [CrossRef] [PubMed]
7. Ebel, B.A.; Romero, O.C.; Martin, D.A. Thresholds and relations for soil-hydraulic and soil-physical properties as a function of burn severity 4 years after the 2011 Las Conchas Fire, New Mexico, USA. *Hydrol. Process.* **2018**, *32*, 2263–2278. [CrossRef]
8. Shakesby, R.A. Post-wildfire soil erosion in the Mediterranean: Review and future research directions. *Earth-Sci. Rev.* **2011**, *105*, 71–100. [CrossRef]
9. Soulis, K.X.; Londra, P.A.; Kargas, G. Characterizing surface soil layer saturated hydraulic conductivity in a Mediterranean natural watershed. *Hydrol. Sci. J.* **2020**, *65*, 2616–2629. [CrossRef]
10. Zhou, Y.; Zhang, Y.; Vaze, J.; Lane, P.; Xu, S. Impact des feux de brousse et de la variabilité climatique sur les débits des bassins versants boisés du Sud-Est Australien. *Hydrol. Sci. J.* **2015**, *60*, 1340–1360. [CrossRef]
11. Poon, P.K.; Kinoshita, A.M. Spatial and temporal evapotranspiration trends after wildfire in semi-arid landscapes. *J. Hydrol.* **2018**, *559*, 71–83. [CrossRef]
12. Vieira, D.C.S.; Malvar, M.C.; Martins, M.A.S.; Serpa, D.; Keizer, J.J. Key factors controlling the post-fire hydrological and erosive response at micro-plot scale in a recently burned Mediterranean forest. *Geomorphology* **2018**, *319*, 161–173. [CrossRef]
13. Fernandez-Manso, A.; Quintano, C.; Roberts, D.A. Burn severity influence on post-fire vegetation cover resilience from Landsat MESMA fraction images time series in Mediterranean forest ecosystems. *Remote Sens. Environ.* **2016**, *184*, 112–123. [CrossRef]
14. Ireland, G.; Petropoulos, G.P. Exploring the relationships between post-fire vegetation regeneration dynamics, topography and burn severity: A case study from the Montane Cordillera Ecozones of Western Canada. *Appl. Geogr.* **2015**, *56*, 232–248. [CrossRef]
15. Keeley, J.E. Fire intensity, fire severity and burn severity: A brief review and suggested usage. *Int. J. Wildl. Fire* **2009**, *18*, 116. [CrossRef]
16. Almalki, R.; Khaki, M.; Saco, P.M.; Rodriguez, J.F. Monitoring and Mapping Vegetation Cover Changes in Arid and Semi-Arid Areas Using Remote Sensing Technology: A Review. *Remote Sens.* **2022**, *14*, 5143. [CrossRef]
17. Rouse, J.W.; Haas, R.H.; Scheel, J.A.; Deering, D.W. Monitoring Vegetation Systems in the Great Plains with ERTS. In *The 3rd Earth Resource Technology Satellite (ERTS) Symposium*; NASA: Washington, DC, USA, 1974.
18. Lacouture, D.L.; Broadbent, E.N.; Crandall, R.M. Detecting Vegetation Recovery after Fire in A Fire-Frequented Habitat Using Normalized Difference Vegetation Index (NDVI). *Forests* **2020**, *11*, 749. [CrossRef]
19. Huete, A.R. A Soil-Adjusted Vegetation Index (SAVI). *Remote Sens. Environ.* **1988**, *25*, 295–308. [CrossRef]
20. Qi, J.; Chehbouni, A.; Huete, A.R.; Kerr, Y.H.; Sorooshian, S. A modified soil adjusted vegetation index. *Remote Sens. Environ.* **1994**, *48*, 119–126. [CrossRef]
21. Veraverbeke, S.; Gitas, I.; Katagis, T.; Polychronaki, A.; Somers, B.; Goossens, R. Assessing post-fire vegetation recovery using red–near infrared vegetation indices: Accounting for background and vegetation variability. *ISPRS J. Photogramm. Remote Sens.* **2012**, *68*, 28–39. [CrossRef]
22. Fabijańczyk, P.; Zawadzki, J. Spatial correlations of NDVI and MSAVI2 indices of green and forested areas of urban agglomeration, case study Warsaw, Poland. *Remote Sens. Appl. Soc. Environ.* **2022**, *26*, 100721. [CrossRef]
23. Schmidt, H.; Karnieli, A. Sensitivity of vegetation indices to substrate brightness in hyper-arid environment: The Makhtesh Ramon Crater (Israel) case study. *Int. J. Remote Sens.* **2001**, *22*, 3503–3520. [CrossRef]
24. Key, C.H.; Benson, N.C. Landscape Assessment (LA) sampling and analysis methods. In *USDA Forest Service–General Technical Report RMRS-GTR*; USDA Forest Service: Fort Collins, CO, USA, 2006.
25. Bright, B.C.; Hudak, A.T.; Kennedy, R.E.; Braaten, J.D.; Khalyani, A.H. Examining post-fire vegetation recovery with Landsat time series analysis in three western North American forest types. *Fire Ecol.* **2019**, *15*, 8. [CrossRef]
26. Chen, X.; Vogelmann, J.E.; Rollins, M.; Ohlen, D.; Key, C.H.; Yang, L.; Huang, C.; Shi, H. Detecting post-fire burn severity and vegetation recovery using multitemporal remote sensing spectral indices and field-collected composite burn index data in a ponderosa pine forest. *Int. J. Remote Sens.* **2011**, *32*, 7905–7927. [CrossRef]
27. Escuin, S.; Navarro, R.; Fernández, P. Fire severity assessment by using NBR (Normalized Burn Ratio) and NDVI (Normalized Difference Vegetation Index) derived from LANDSAT TM/ETM images. *Int. J. Remote Sens.* **2008**, *29*, 1053–1073. [CrossRef]
28. Veraverbeke, S.; Lhermitte, S.; Verstraeten, W.W.; Goossens, R. A time-integrated MODIS burn severity assessment using the multi-temporal differenced normalized burn ratio (dNBRMT). *Int. J. Appl. Earth Obs. Geoinf.* **2011**, *13*, 52–58. [CrossRef]
29. Papathanasiou, C.; Makropoulos, C.; Mimikou, M. Hydrological modelling for flood forecasting: Calibrating the post-fire initial conditions. *J. Hydrol.* **2015**, *529*, 1838–1850. [CrossRef]
30. Carreño-Conde, F.; Sipols, A.E.; de Blas, C.S.; Mostaza-Colado, D. A Forecast Model Applied to Monitor Crops Dynamics Using Vegetation Indices (NDVI). *Appl. Sci.* **2021**, *11*, 1859. [CrossRef]
31. Xu, B.; Lin, B. Assessing CO_2 emissions in China's iron and steel industry: A dynamic vector autoregression model. *Appl. Energy* **2016**, *161*, 375–386. [CrossRef]

32. Ramli, I.; Rusdiana, S.; Basri, H.; Munawar, A.A. VAzelia Predicted Rainfall and Discharge Using Vector Autoregressive Models in Water Resources Management in the High Hill Takengon. *IOP Conf. Ser. Earth Environ. Sci.* **2019**, *273*, 012009. [CrossRef]
33. Pan, X.; Jarrett, J.E. Why and how to use vector autoregressive models for quality control: The guideline and procedures. *Qual. Quant.* **2012**, *46*, 935–948. [CrossRef]
34. Lee, R.J.; Chow, T.E. Post-wildfire assessment of vegetation regeneration in Bastrop, Texas, using Landsat imagery. *GIScience Remote Sens.* **2015**, *52*, 609–626. [CrossRef]
35. Lucas-Borja, M.E.; Bombino, G.; Carrà, B.G.; D'Agostino, D.; Denisi, P.; Labate, A.; Plaza-Alvarez, P.A.; Zema, D.A. Modeling the Soil Response to Rainstorms after Wildfire and Prescribed Fire in Mediterranean Forests. *Climate* **2020**, *8*, 150. [CrossRef]
36. Lucas-Borja, M.E.; Plaza-Alvarez, P.A.; Xu, X.; Carra, B.G.; Zema, D.A. Exploring the factors influencing the hydrological response of soil after low and high-severity fires with post-fire mulching in Mediterranean forests. *Int. Soil Water Conserv. Res.* **2023**, *11*, 169–182. [CrossRef]
37. Keizer, J.J.; Silva, F.C.; Vieira, D.C.S.; González-Pelayo, O.; Campos, I.; Vieira, A.M.D.; Valente, S.; Prats, S.A. The effectiveness of two contrasting mulch application rates to reduce post-fire erosion in a Portuguese eucalypt plantation. *CATENA* **2018**, *169*, 21–30. [CrossRef]
38. Lentile, L.B.; Holden, Z.A.; Smith, A.M.S.; Falkowski, M.J.; Hudak, A.T.; Morgan, P.; Lewis, S.A.; Gessler, P.E.; Benson, N.C. Remote sensing techniques to assess active fire characteristics and post-fire effects. *Int. J. Wildl. Fire* **2006**, *15*, 319. [CrossRef]
39. Delgado-Aguilar, M.J.; Hinojosa, L.; Schmitt, C.B. Combining remote sensing techniques and participatory mapping to understand the relations between forest degradation and ecosystems services in a tropical rainforest. *Appl. Geogr.* **2019**, *104*, 65–74. [CrossRef]
40. Fernández, C.; Vega, J.A.; Vieira, D.C.S. Assessing soil erosion after fire and rehabilitation treatments in NW Spain: Performance of rusle and revised Morgan-Morgan-Finney models. *Land Degrad. Dev.* **2010**, *21*, 58–67. [CrossRef]
41. Havel, A.; Tasdighi, A.; Arabi, M. Assessing the hydrologic response to wildfires in mountainous regions. *Hydrol. Earth Syst. Sci.* **2018**, *22*, 2527–2550. [CrossRef]
42. Renard, K.G.; Foster, G.R.; Weesies, G.A.; McCool, D.K.; Yoder, D.C. *Predicting Soil Erosion by Water: A Guide to Conservation Planning with the Revised Universal Soil Loss Equation (RUSLE)*; United States Departments of Agriculture USDA: Washington, DC, USA, 1997; p. 49.
43. Morgan, R.P.C. A simple approach to soil loss prediction: A revised Morgan-Morgan-Finney model. *Catena* **2001**, *44*, 305–322. [CrossRef]
44. Kirkby, M.J.; Jones, R.J.A.; Irvine, B.; Gobin, A.; Govers, G.; Cerdan, O.; Van Rompaey, A.J.J.; Le Bissonnais, Y.; Daroussin, J.; King, D.; et al. *Pan-European Soil Erosion Risk Assessment: The PESERA Map*; European Commission: Brussel, Belgium, 2004.
45. Arnold, J.G.; Moriasi, D.N.; Gassman, P.W.; Abbaspour, K.C.; White, M.J.; Srinivasan, R.; Santhi, C.; Harmel, R.D.; Van Griensven, A.; Van Liew, M.W.; et al. SWAT: Model Use, Calibration, and Validation. *Trans. ASABE* **2012**, *55*, 1491–1508. [CrossRef]
46. Vieira, D.C.S.; Malvar, M.C.; Fernández, C.; Serpa, D.; Keizer, J.J. Annual runoff and erosion in a recently burn Mediterranean forest—The effects of plowing and time-since-fire. *Geomorphology* **2016**, *270*, 172–183. [CrossRef]
47. Rulli, M.C.; Offeddu, L.; Santini, M. Modeling post-fire water erosion mitigation strategies. *Hydrol. Earth Syst. Sci.* **2013**, *17*, 2323–2337. [CrossRef]
48. Fernández, C.; Vega, J.A. Evaluation of RUSLE and PESERA models for predicting soil erosion losses in the first year after wildfire in NW Spain. *Geoderma* **2016**, *273*, 64–72. [CrossRef]
49. Nunes, J.P.; Quintanilla, P.N.; Santos, J.M.; Serpa, D.; Carvalho-Santos, C.; Rocha, J.; Keizer, J.J.; Keesstra, S.D. Afforestation, Subsequent Forest Fires and Provision of Hydrological Services: A Model-Based Analysis for a Mediterranean Mountainous Catchment. *Land Degrad. Dev.* **2018**, *29*, 776–788. [CrossRef]
50. Soulis, K.X.; Generali, K.A.; Papadaki, C.; Theodoropoulos, C.; Psomiadis, E. Hydrological Response of Natural Mediterranean Watersheds to Forest Fires. *Hydrology* **2021**, *8*, 15. [CrossRef]
51. Papavasileiou, G.; Giannaros, T.M. The Catastrophic 2021 Wildfires in Greece: An Outbreak of Pyroconvective Events. In Proceedings of the Third International Conference on Fire Behavior and Risk ICFBR, Sardinia, Italy, 3–6 May 2022; p. 7.
52. Karali, A.; Varotsos, K.V.; Giannakopoulos, C.; Nastos, P.P.; Hatzaki, M. Seasonal fire danger forecasts for supporting fire prevention management in an eastern Mediterranean environment: The case of Attica, Greece. *Nat. Hazards Earth Syst. Sci.* **2023**, *23*, 429–445. [CrossRef]
53. Giannaros, T.M.; Papavasileiou, G.; Lagouvardos, K.; Kotroni, V.; Dafis, S.; Karagiannidis, A.; Dragozi, E. Meteorological Analysis of the 2021 Extreme Wildfires in Greece: Lessons Learned and Implications for Early Warning of the Potential for Pyroconvection. *Atmosphere* **2022**, *13*, 475. [CrossRef]
54. Falaras, T.; Tselka, I.; Papadopoulos, I.; Nikolidaki, M.; Karavias, A.; Bafi, D.; Petani, A.; Krassakis, P.; Parcharidis, I. Operational Mapping and Post-Disaster Hazard Assessment by the Development of a Multiparametric Web App Using Geospatial Technologies and Data: Attica Region 2021 Wildfires (Greece). *Appl. Sci.* **2022**, *12*, 7256. [CrossRef]
55. Mamassis, N.; Koukouvinos, A.; Baki, S. Development of a Geographical Information System and an Internet application for the supervision of Kephisos Protected Areas Department of Water Resources and Environmental Engineering. Master's Thesis, National Technical University of Athens, Athens, Greece, 2008. Available online: http://www.itia.ntua.gr/el/project_reports/151/ (accessed on 20 December 2020).

56. Zerefos, C.; Repapis, C.; Giannakopoulos, C.; Kapsomenakis, J.; Papanikolaou, D.; Papanikolaou, M.; Poulos, S.; Vrekoussis, M.; Philandras, C.; Tselioudis, G. The Climate of the Eastern Mediterranean and Greece: Past, Present and Future. In *the Environmental, Economic and Social Impacts of Climate Changing Greece*; Bank of Greece: Athens, Greece, 2011; pp. 50–58.
57. Lagouvardos, K.; Kotroni, V.; Bezes, A.; Koletsis, I.; Kopania, T.; Lykoudis, S.; Mazarakis, N.; Papagiannaki, K.; Vougioukas, S. The automatic weather stations NOANN network of the National Observatory of Athens: Operation and database. *Geosci. Data J.* **2017**, *4*, 4–16. [CrossRef]
58. FAO; IIASA; ISRIC; ISSCAS. *Harmonized World Soil Database Version 1.2*; Food & Agriculture Organization of the UN: Rome, Italy; International Institute for Applied Systems Analysis: Laxenburg, Austria, 2012; ISBN 9781626239777.
59. Corine Land Cover (CLC). Land Use Data. Available online: https://land.copernicus.eu/ (accessed on 15 December 2020).
60. Evelpidou, N.; Tzouxanioti, M.; Gavalas, T.; Spyrou, E.; Saitis, G.; Petropoulos, A.; Karkani, A. Assessment of Fire Effects on Surface Runoff Erosion Susceptibility: The Case of the Summer 2021 Forest Fires in Greece. *Land* **2021**, *11*, 21. [CrossRef]
61. U.S. Geological Survey (USGS). Shuttle Radar Topography Mission (SRTM) Global, DEM Data, Open Topography. Available online: https://earthexplorer.usgs.gov/ (accessed on 5 December 2020).
62. Mamassis, N.; Mazi, K.; Dimitriou, E.; Kalogeras, D.; Malamos, N.; Lykoudis, S.; Koukouvinos, A.; Tsirogiannis, I.; Papageorgaki, I.; Papadopoulos, A.; et al. OpenHi.net: A Synergistically Built, National-Scale Infrastructure for Monitoring the Surface Waters of Greece. *Water* **2021**, *13*, 2779. [CrossRef]
63. Gorelick, N.; Hancher, M.; Dixon, M.; Ilyushchenko, S.; Thau, D.; Moore, R. Google Earth Engine: Planetary-scale geospatial analysis for everyone. *Remote Sens. Environ.* **2017**, *202*, 18–27. [CrossRef]
64. Chander, G.; Markham, B.; Helder, D.L. Summary of current radiometric calibration coefficients for Landsat MSS, TM, ETM+, and EO-1 ALI sensors. *Remote Sens. Environ.* **2009**, *113*, 893–903. [CrossRef]
65. García, M.J.L.; Caselles, V. Mapping burns and natural reforestation using thematic mapper data. *Geocarto Int.* **1991**, *6*, 31–37. [CrossRef]
66. Miller, J.D.; Thode, A.E. Quantifying burn severity in a heterogeneous landscape with a relative version of the delta Normalized Burn Ratio (dNBR). *Remote Sens. Environ.* **2007**, *109*, 66–80. [CrossRef]
67. Pettorelli, N.; Vik, J.O.; Mysterud, A.; Gaillard, J.M.; Tucker, C.J.; Stenseth, N.C. Using the satellite-derived NDVI to assess ecological responses to environmental change. *Trends Ecol. Evol.* **2005**, *20*, 503–510. [CrossRef]
68. Sims, C.A. Interpreting the macroeconomic time series facts. *Eur. Econ. Rev.* **1992**, *36*, 975–1000. [CrossRef]
69. Gao, J.; Peng, B.; Yan, Y. Estimation, Inference, and Empirical Analysis for Time-Varying VAR Models. *J. Bus. Econ. Stat.* **2024**, *42*, 310–321. [CrossRef]
70. Athanasopoulos, G.; Poskitt, D.S.; Vahid, F. Two canonical VARMA forms: Scalar component models vis-à-vis the Echelon form. *Econom. Rev.* **2012**, *31*, 60–83. [CrossRef]
71. Hacker, R.S.; Hatemi-J, A. Optimal lag-length choice in stable and unstable VAR models under situations of homoscedasticity and ARCH. *J. Appl. Stat.* **2008**, *35*, 601–615. [CrossRef]
72. Moritz, S.; Bartz-Beielstein, T. imputeTS: Time series missing value imputation in R. *R J.* **2017**, *9*, 207–218. [CrossRef]
73. Dickey, D.A.; Fuller, W.A. Distribution of the Estimators for Autoregressive Time Series With a Unit Root. *J. Am. Stat. Assoc.* **1979**, *74*, 427. [CrossRef]
74. Arnold, J.G.; Srinivasan, R.; Muttiah, R.S.; Williams, J.R. Large Area Hydrologic Modeling and Assessment Part I: Model Development. *J. Am. Water Resour. Assoc.* **1998**, *34*, 73–89. [CrossRef]
75. Neitsch, S.L.; Arnold, J.G.; Kiniry, J.R.; Srinivasan, R.; Williams, J.R. *Soil and Water Assessment Tool Theoretical Documentation: Version 2009*; Texas Water Resources Institute Technical Report 406; Texas A&M University System: College Station, TX, USA, 2011.
76. Tan, M.L.; Gassman, P.W.; Yang, X.; Haywood, J. A review of SWAT applications, performance and future needs for simulation of hydro-climatic extremes. *Adv. Water Resour.* **2020**, *143*, 103662. [CrossRef]
77. Gassman, P.W.; Sadeghi, A.M.; Srinivasan, R. Applications of the SWAT Model Special Section: Overview and Insights. *J. Environ. Qual.* **2014**, *43*, 1–8. [CrossRef]
78. Dile, Y.T.; Daggupati, P.; George, C.; Srinivasan, R.; Arnold, J. Introducing a new open source GIS user interface for the SWAT model. *Environ. Model. Softw.* **2016**, *85*, 129–138. [CrossRef]
79. Soil Conservation Service. *National Engineering Handbook, Section 4, Hydrology*; Department of Agriculture: Washington, DC, USA, 1972.
80. Mein, R.G.; Larson, C.L. Modeling Infiltration during a Steady Rain. *Water Resour. Res.* **1973**, *9*, 384–394. [CrossRef]
81. Abbaspour, K.C.; Yang, J.; Maximov, I.; Siber, R.; Bogner, K.; Mieleitner, J.; Zobrist, J.; Srinivasan, R. Modelling hydrology and water quality in the pre-alpine/alpine Thur watershed using SWAT. *J. Hydrol.* **2007**, *333*, 413–430. [CrossRef]
82. Moriasi, D.N.; Gitau, M.W.; Pai, N.; Daggupati, P. Hydrologic and water quality models: Performance measures and evaluation criteria. *Trans. ASABE* **2015**, *58*, 1763–1785. [CrossRef]
83. Larsen, I.J.; MacDonald, L.H. Predicting postfire sediment yields at the hillslope scale: Testing RUSLE and Disturbed WEPP. *Water Resour. Res.* **2007**, *43*, 1–18. [CrossRef]
84. Boucher, J.; Beaudoin, A.; Hébert, C.; Guindon, L.; Bauce, É. Assessing the potential of the differenced Normalized Burn Ratio (dNBR) for estimating burn severity in eastern Canadian boreal forests. *Int. J. Wildl. Fire* **2017**, *26*, 32. [CrossRef]

85. Lütkepohl, H. Vector autoregressive models. In *Handbook of Research Methods and Applications in Empirical Macroeconomics*; Hashimzade, N., Thorntopn, M.A., Eds.; Edward Elgar Publishing: Cheltenham, UK, 2013; pp. 139–164. [CrossRef]
86. Arianoutsou, M.; Christopoulou, A.; Kazanis, D.; Tountas, T.; Ganou, E.; Bazos, I. Effects of Fire on High Altitude Coniferous Forests of Greece. In Proceedings of the VI International Conference on Forest Fire Research, Coimbra, Portugal, 15–18 November 2010; pp. 1–13.
87. Di Piazza, G.V.; Di Stefano, C.; Ferro, V. Modelling the effects of a bushfire on erosion in a Mediterranean basin/Modélisation des impacts d'un incendie sur l'érosion dans un bassin Méditerranéen. *Hydrol. Sci. J.* **2007**, *52*, 1253–1270. [CrossRef]
88. Koltsida, E.; Mamassis, N.; Kallioras, A. Hydrological modeling using the Soil and Water Assessment Tool in urban and peri-urban environments: The case of Kifisos experimental subbasin (Athens, Greece). *Hydrol. Earth Syst. Sci.* **2023**, *27*, 917–931. [CrossRef]
89. King, K.W.; Arnold, J.G.; Bingner, R.L. Comparison of Green-Ampt and curve number methods on Goodwin Creek Watershed using SWAT. *Trans. Am. Soc. Agric. Eng.* **1999**, *42*, 919–925. [CrossRef]
90. Jeong, J.; Kannan, N.; Arnold, J.; Glick, R.; Gosselink, L.; Srinivasan, R. Development and Integration of Sub-hourly Rainfall-Runoff Modeling Capability Within a Watershed Model. *Water Resour. Manag.* **2010**, *24*, 4505–4527. [CrossRef]
91. Kannan, N.; White, S.M.; Worrall, F.; Whelan, M.J. Sensitivity analysis and identification of the best evapotranspiration and runoff options for hydrological modelling in SWAT-2000. *J. Hydrol.* **2007**, *332*, 456–466. [CrossRef]
92. Bauwe, A.; Kahle, P.; Lennartz, B. Hydrologic evaluation of the curve number and Green and Ampt infiltration methods by applying Hooghoudt and Kirkham tile drain equations using SWAT. *J. Hydrol.* **2016**, *537*, 311–321. [CrossRef]
93. Shakesby, R.; Doerr, S. Wildfire as a hydrological and geomorphological agent. *Earth-Sci. Rev.* **2006**, *74*, 269–307. [CrossRef]
94. Liu, S.; Leslie, L.M.; Speer, M.; Bunker, R.; Mo, X. The effects of bushfires on hydrological processes using a paired-catchment analysis. *Meteorol. Atmos. Phys.* **2004**, *86*, 31–44. [CrossRef]
95. Scott, D.F.; Versfeld, D.B.; Lesgh, W. Erosion and Sediment Yield in Relation to Afforestation and Fire in the Mountains of the Western Cape Province, South Africa. *S. Afr. Geogr. J.* **1998**, *80*, 52–59. [CrossRef]
96. Rodrigues, E.L.; Jacobi, C.M.; Figueira, J.E.C. Wildfires and their impact on the water supply of a large neotropical metropolis: A simulation approach. *Sci. Total Environ.* **2019**, *651*, 1261–1271. [CrossRef]
97. Wijesekara, G.N.; Gupta, A.; Valeo, C.; Hasbani, J.-G.; Qiao, Y.; Delaney, P.; Marceau, D.J. Assessing the impact of future land-use changes on hydrological processes in the Elbow River watershed in southern Alberta, Canada. *J. Hydrol.* **2012**, *412–413*, 220–232. [CrossRef]
98. Wilder, B.A.; Kinoshita, A.M. Post-Fire Vegetation and Hydrologic Recovery in a Mediterranean Climate. In Proceedings of the AGU Fall Meeting, Virtual, 1–17 December 2020.
99. Hernández-Duarte, A.; Saavedra, F.; González, E.; Miranda, A.; Francois, J.; Somos-Valenzuela, M.; Sibold, J. Effects of Drought and Fire Severity Interaction on Short-Term Post-Fire Recovery of the Mediterranean Forest of South America. *Fire* **2024**, *7*, 428. [CrossRef]
100. Abbaspour, K.C.; Rouholahnejad, E.; Vaghefi, S.; Srinivasan, R.; Yang, H.; Kløve, B. A continental-scale hydrology and water quality model for Europe: Calibration and uncertainty of a high-resolution large-scale SWAT model. *J. Hydrol.* **2015**, *524*, 733–752. [CrossRef]
101. Kamali, B.; Abbaspour, K.; Yang, H. Assessing the Uncertainty of Multiple Input Datasets in the Prediction of Water Resource Components. *Water* **2017**, *9*, 709. [CrossRef]
102. Guzman, J.A.; Shirmohammadi, A.; Sadeghi, A.M.; Wang, X.; Chu, M.L.; Jha, M.K.; Parajuli, P.B.; Harmel, R.D.; Khare, Y.P.; Hernandez, J.E. Uncertainty considerations in calibration and validation of hydrologic and water quality models. *Trans. ASABE* **2015**, *58*, 1745–1762. [CrossRef]
103. Google Earth Engine. Landsat Algorithms—Earth Engine. Available online: https://developers.google.com/earth-engine/guides/landsat (accessed on 12 December 2024).